PURDUE UNIVERSITY
HYDROMECHANICS LAB
SCHOOL OF CIVIL ENGINEERING

A Study of the Flow Structure of Tip Vortices on a Hydrofoil

REPORT DOCUMENTATION PAGE

PORT SECURITY CLASSIFICATION UNCLASSIFIED	1b RESTRICTIVE MARKINGS
CURITY CLASSIFICATION AUTHORITY	3 DISTRIBUTION / AVAILABILITY OF REPORT Approved for public release, Distribution unlimited
CLASSIFICATION / DOWNGRADING SCHEDULE	
FORMING ORGANIZATION REPORT NUMBER(S) CE-HSE-86-20	5. MONITORING ORGANIZATION REPORT NUMBER(S) CE-HSE-86-20
AME OF PERFORMING ORGANIZATION Purdue Research Foundation Purdue University 6b. OFFICE SYMBOL (If applicable)	7a. NAME OF MONITORING ORGANIZATION Office of Naval Research
DDRESS (City, State, and ZIP Code) School of Civil Engineering West Lafayette, Indiana 47907	7b. ADDRESS (City, State, and ZIP Code) Arlington, Virginia 22217-5000
AME OF FUNDING / SPONSORING RGANIZATION 1 Sea Sys. Comd. (DTNSRDC) 8b. OFFICE SYMBOL (If applicable)	9. PROCUREMENT INSTRUMENT IDENTIFICATION NUMBER N00014-85-K-0106 N00167-86-K-0018
DDRESS (City, State, and ZIP Code) Bethesda, Maryland	10 SOURCE OF FUNDING NUMBERS PROGRAM ELEMENT NO / PROJECT NO. / TASK NO. / WORK UNIT ACCESSION NO

TLE (Include Security Classification)

A Study of the Flow Structure of Tip Vortices on a Hydrofoil (Unclassified)

ERSONAL AUTHOR(S)

Thomas B. Francis, (Joseph Katz, Project Director)

TYPE OF REPORT	13b. TIME COVERED	14. DATE OF REPORT (Year, Month, Day)	15. PAGE COUNT
Technical	FROM 11/84 TO 11/86	1986/11/28	126

UPPLEMENTARY NOTATION

COSATI CODES			18. SUBJECT TERMS (Continue on reverse if necessary and identify by block number)
IELD	GROUP	SUB-GROUP	
			Hydrofoils, Tip Vortices, Flow Visualization, Towing Tanks, Laser Induced Fluorescence, Surface Pressure.

BSTRACT (Continue on reverse if necessary and identify by block number)

A detailed study of the tip vortices generated on a NACA-66 series hydrofoil is erformed in the Purdue University towing tank. The investigation involves flow isualization experiments and pressure measurements performed under various test onditions.

Laser induced fluorescence is utilized as the means of flow visualization. An rgon ion laser beam is expanded into a thin sheet of light, which in turn slices a ertical and lateral cross section of the flow field. Rhodamine dye is introduced into ie field, either by injecting it from the surface of the model. As the model is towed irough the tank, the dye becam visible in the section illuminated by the laser sheet. ie resulting image showed the vortex structure at that region, unobstructed by the est of the flow. This image is recorded by a television camera which trails behind ie model.

(continued on supplement page).

ISTRIBUTION / AVAILABILITY OF ABSTRACT UNCLASSIFIED/UNLIMITED ☐ SAME AS RPT ☐ DTIC USERS	21 ABSTRACT SECURITY CLASSIFICATION
NAME OF RESPONSIBLE INDIVIDUAL J. Monacella	22b. TELEPHONE (Include Area Code) / 22c. OFFICE SYMBOL

ORM 1473, 84 MAR 83 APR edition may be used until exhausted. All other editions are obsolete. SECURITY CLASSIFICATION OF THIS PAGE

19. ABSTRACT (Continued)

Pressure measurements are performed by using a system which includes a scanning valve and a pneumatic control mechanism. Ports are located on the model surface from which pressure information is obtained. The extensive number of ports warrants the use of a scanning valve, which provides rapid and efficient measurements. The pneumatic control device is necessary for data collection. Once collected, the information is routed through an analog to digital converter and sent to a personal computer to be stored and analyzed.

Results obtained from the flow visualization experiments show several clear trends. First, the size of the tip vortex increases as it develops downstream along the hydrofoil chord. Second, the size of the tip vortex increases and its center line becomes more detached as the angle of attack is increased. Third, the tip vortex experiences a size reduction and an outward center line shift as the speed (Reynolds Number) increases. In addition, secondary structures including shear layer eddies are clearly visible in most flow visualization images.

Results obtained from the pressure measurements are used to obtain a correlation between the surface pressure distribution and the tip vortex development. They are also used to determine the spanwise pressure gradients causing the roll up of the tip vortex, and to locate regions of boundary layer separation.

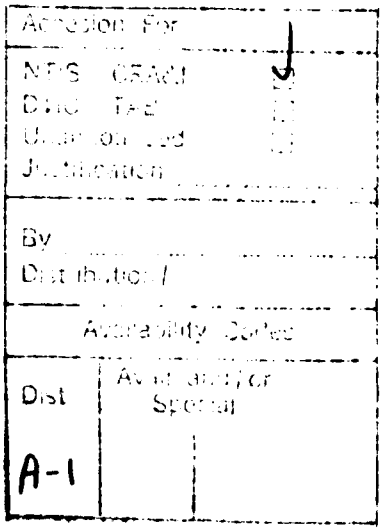

A STUDY OF THE FLOW STRUCTURE OF TIP VORTICES ON A HYDROFOIL

A Thesis

Submitted to the Faculty

of

Purdue University

by

Thomas B. Francis

In Partial Fulfillment of the

Requirements for the Degree

of

Masters of Science in Civil Engineering

December 1986

This thesis is dedicated to my friends and family. Yes mom, I finally finished my thesis!

ACKNOWLEDGEMENTS

I would like to thank Professor Joseph Katz, who gave me the opportunity to work on the project on which this research is based. Working under him was a unique learning experience.

I'd also like to thank David Cochran, Kenneth Ward, and Todd Fawver for their help with my research. I'd especially like to thank James T. Craig for his help during the construction of the hydrofoil, and Thomas Cooper for his help during the testing period.

The research is sponsored by the Naval Sea Systems Command, administered by the David Taylor Naval Ship Research and Development Center under contract number N00014-85-K-0106. Their support is gratefully acknowledged.

TABLE OF CONTENTS

LIST OF TABLES

LIST OF FIGURES

LIST OF SYMBOLS

Symbol	Description
C	Chord length
C_L	Lift coefficient
C_p	Pressure coefficient, which equals $\frac{P - P_\infty}{\frac{1}{2} \rho V^2}$
D	Tip vortex characteristic size
L	Lift
LS	Horizontal distance between the wing's tip and the attachment line
LY	Vertical distance between the wing's tip and the center of the vortex
LZ	Horizontal distance between the wing's tip and the center of the vortex
P_c	Pressure in the core of a Rankine Vortex
P_v	Vapor pressure
P_∞	Pressure (at infinity)
r_c	Radius of the core of a Rankine Vortex
Re_c	Reynolds Number, which equals VC/ν
S	Span length
V	Free stream velocity
V_θ	Tangential velocity

Symbol	Description
X	Chordwise position
Z	Spanwise position
α	Incidence angle
Γ	Circulation
π	Pi = 3.1416
ρ	Liquid density
σ_i	Cavitation inception index

ABSTRACT

Francis, Thomas Bert., MSCE., Purdue University, December 1986., A Study of the Flow Structure of Tip Vortices on a Hydrofoil. Major Professor: Joseph Katz.

A detailed study of the tip vortices generated on a NACA-66 series hydrofoil is performed in the Purdue University towing tank. The investigation involves flow visualization experiments and pressure measurements performed under various test conditions.

Laser induced fluorescence is utilized as the means of flow visualization. An argon ion laser beam is expanded into a thin sheet of light, which in turn slices a vertical and lateral cross section of the flow field. Rhodamine dye is introduced into the field, either by injecting it from the surface of the model, or by seeding it in a section of the water upstream of the model. As the model is towed through the tank, the dye became visible in the section illuminated by the laser sheet. The resulting image showed the vortex structure at that region, unobstructed by the rest of the flow. This image is recorded by a television camera which trails behind the model.

Pressure measurements are performed by using a system which includes a scanning valve and a pneumatic control mechanism. Ports are located on the model surface from which pressure information is obtained. The extensive number of ports warrants the use of a scanning valve, which provides rapid and efficient measurements. The pneumatic control device is necessary for data collection. Once collected, the information is routed through an analog to digital converter and sent to a personal computer to be stored and analyzed.

Results obtained from the flow visualization experiments show several clear trends. First, the size of the tip vortex increases as it develops downstream along the hydrofoil chord. Second, the size of the tip vortex increases and its center line becomes more detached as the angle of attack is increased. Third, the tip vortex experiences a size reduction and an outward center line shift as the speed (Reynolds Number) increases. In addition, secondary structures including shear layer eddies are clearly visible in most flow visualization images.

Results obtained from the pressure measurements are used to obtain a correlation between the surface pressure distribution and the tip vortex development. They are also used to determine the spanwise pressure gradients causing

the roll up of the tip vortex, and to locate regions of boundary layer separation.

CHAPTER 1 - LITERATURE SURVEY

1.1 Introduction

The literature survey is divided into seven sections. The second, third, and fourth sections provide background information, describe theoretical models, and review experimental studies, respectively. Tip vortex cavitation and vortex alleviation techniques are discussed in the fifth and sixth sections. Finally, the seventh section presents the rationale for the current study.

1.2 Background

Trailing and tip vortices are formed on a lifting surface of finite span since the existing pressure difference between the two sides of its surface must disappear at the tip. This reasoning explains why spanwise pressure gradients of opposite sign exist on both sides of an airfoil. These gradients induce an inward lateral flow on the suction side and an outward lateral flow on the pressure side of the foil. When these flows meet near the tip of the foil, a trailing vortex is formed (see figure I.1). This vortex can cause severe problems in many applications of

lifting surfaces. For example, the vortex trailing a helicopter blade will affect the performance of the blade that follows, trailing vortices produced by large planes pose a hazard to small planes passing through them, and the susceptibility of the low pressure region in the vortex core to cavitate contributes to noise, vibration, and erosion in pump and marine propeller applications. As a result, many studies have been performed to investigate tip vortices, the associated scaling trends, and the various means for alleviating their effects. Platzer and Sounders (1979) gathered the pertinent work performed and summarized approximately 150 publications. Of these reports, around eighty percent dealt with problems encountered in the aircraft industry, and thus concentrated on the wake behind a wing, particularly the far field phenomena. The region of cavitation inception, namely the roll up region near the tip, received much less attention. Consequently, further study in this area is needed.

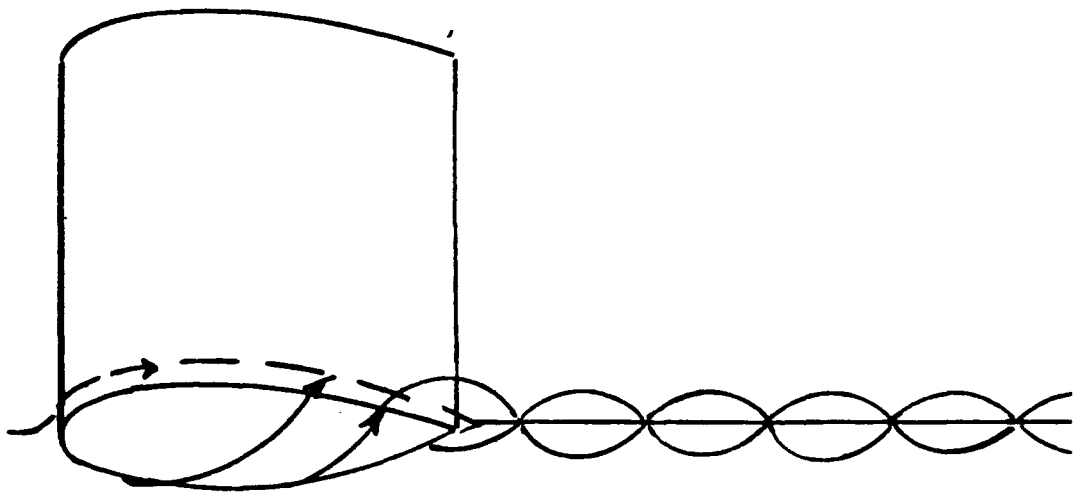

Figure I.1 A sketch illustrating the tip vortex roll up process.

1.3 Models developed to predict vortex growth

Several attempts have been made to accurately describe the tip vortex roll up process. Lamb (1932) was the first to develop a simplified inviscid description of the phenomenon. His model consisted of a concentrated vortex whose strength depended on the spanwise load distribution over the wing. Through the years, other researchers have used this model as a base for their work. For example, Batchelor (1964) modified the model by introducing three dimensionality to the flow. This improvement was accomplished by including axial velocity in the analysis. Moore and Shaffman (1973) further revised the model by including the effects of viscosity on the vortex structure.

In addition to Lamb, Betz (1932) is recognized as a pioneer in this area. He was the first to develop a model to describe trailing vortices. Using the momentum equation of an inviscid fluid, he related the structure of the vortex sheet behind an isolated wing to the structure of a single fully developed vortex. Forty years later, Donaldson et al.(1971,1973) and Donaldson and Bilanin (1975) demonstrated that a single rolled-up vortex could not exist in the immediate vicinity of the lifting surface, and proceeded to develop a criterion for estimating the number of vortices based on the load distribution. Yates (1974) used this technique in his study of the wake created behind

airplanes during take off and landing. It gave a reasonable prediction of the strength and location of the trailing vortices. Bilanin et. al. (1977) used the Betz model in studies of trailing vortices and found that it worked quite well as long as the individual vortices did not merge. This finding led to their development of a computer code to model trailing vortices which took the merging into account. Additionally, they showed that a substantial reduction of wake hazards could be achieved through the generation of multiple vortices using proper wing flap configuration. This conclusion supported previous experimental observations by Corsiglia et. al. (1976) who studied the effect of various flap configurations on the generated vortices.

Recently, numerical studies have been performed as an approach to the problem. Shamroth and Gibeling (1979) used the Navier Stokes equation to describe turbulent flow over an aircraft. Using the Navier Stokes equation allowed the effects of differing wing tip geometries, viscosity values, and turbulence conditions on the roll up process to be included in the model. Chen and Wu (1983) developed a three dimensional finite element method utilizing a system of bound vortices with vortex lattices to represent wing, jet-wake, and tip vortices. Mansour (1984) conducted an intensive numerical study in an attempt to model the tip vortex formation on low aspect ratio wings in subsonic and

transonic velocity ranges. And most recently, Cebeci et al. (1986) developed a viscous/inviscid interaction method to calculate the flow around airfoils, emphasizing the separation region and the resulting wake. They found that their results were good for thin airfoils. However, they deteriorated appreciably as the foil thickness increased. Unfortunately, their findings are consistent with those of others who use numerical schemes, in that the models developed work well in some situations, but not under wide ranges of operating speeds and foil configurations.

Although it is obvious that many attempts have been made and will continue to be made to model the roll up process of tip vortices, it is also clear that their success is modest at best. Currently, researchers have been unable to obtain an accurate estimate of the effect that changes in the load distribution of the wing tip geometry have on the roll up process. Numerical solution schemes such as those by Mansour (1984) and Cebeci et al. (1986) continue to be refined in order to obtain better solutions.

1.4 Experimental studies of tip vortices, including those done on parameters that affect the vortex growth

Since the mid sixties, there has been a marked increase in the number of experiments performed on tip vortices. As mentioned previously, a majority of these tests

involve the aircraft industry, and thus focus on the wake behind a wing. A review of the research and development work conducted on aircraft wake vortices was carried out by Hallock and Eberle (1977). The review included research done on the vortex roll up phenomena, vortex transport, vortex decay, wake minimization, and hazards associated with the vortex. It also provided information that dealt with what was then the ongoing research in these areas.

As listed in Hallock and Eberle's review, there have been hundreds of studies performed on wake vortices in the past. Several of these studies are significant, and merit discussion. McCormick et al. (1968) conducted a series of experiments involving full scale and model testing of the wake behind a wing. Their aim was to develop a predictive method that could be used to determine the vortex geometry and velocity downstream of an aircraft. In the course of his study, measurements taken inside the wake region were used to show that the tangential velocity in the vortex core decreased and the core dimensions increased as the vortex progressed further downstream from the foil. They also found that circulation at the core remained constant with downstream distance, and was equal to just a fraction (16%) of the total strength of the vortex. Continued experiments were performed by Mertaugh et. al. (1977). They were mainly concerned with obtaining near-field velocity measurements in the wake region. The findings

demonstrated that the vorticity generated at the trailing edge of a wing tended to roll up into a single vortex core. They also showed that for relatively high aspect ratio wings, inviscid theory gave a good estimation of the rate of roll up. However, they went on to state that this approach could not be used to provide any insight into the role that various viscous and turbulent effects have on this process. El-Ramly and Rainbird (1977) also performed a major study on the wake behind a foil. This study demonstrated that within the range of experiments (up to 13 times the wing span) the vorticity shed at the trailing edge of a wing was never fully rolled up into a single concentrated vortex. Specifically, there was a 74% roll up in rectangular wing testing, and a 60% roll up in swept wing applications. Their studies led them to conclude that the strength of the tip vortex depended strongly on the spanwise distribution, or more accurately on rapid variation of the loading and the nature of boundary layer separation near the tip. They also compared their results with the Betz model, finding reasonable agreement in the vortex viscous core area. However, outside that region, the model deteriorated due to the assumption that the roll up was complete, when, in fact, it wasn't. Agreement also was poor near the vortex center, due to the strong viscous effects that exist there.

Several others have conducted experimental investigations which add to the understanding of the vortex structure. Ciffone (1974) measured the axial velocity defect in the cores of trailing vortices. The data collected was used to help describe the vortex behavior in the region ranging from 10 chord lengths to 35 chord lengths downstream of the foil. Thompson (1975) conducted a study of the axial velocity distribution in wing tip vortices. His major finding was that the tip edge shape played a deciding role in determining this distribution. Grow (1969) measured the tangential velocity of the tip vortex near the tip of the wing. He observed that boundary layer tripping resulted in a substantial increase in the core radius and a decrease in tangential velocity. Detailed velocity measurements were also carried out by Corsiglia et al. (1973) who identified an inner rotational vortex core in which the velocity grew with the radius and an outer irrotational region. This study was followed by Francis (1976) whose velocity measurements demonstrated that the vorticity generated by the boundary layer on the pressure side of the wing migrated around the tip to the suction side. This vorticity and the external flow field induced an outward flow near the tip of the suction side of the wing. Sounders and Platzer (1981) confirmed the existence of the outward flow through surface-oil-flow-visualization studies.

Research conducted in the nineteen eighties has improved upon that of the past due to the advances made in visualizing flows and measuring velocities. Some of the most active experimenters in this area are Freymuth,Bank, and Palmer (1984, 1985), Freymuth, Bank, and Finaish (1985,1986), and Higuchi et. al. (1985, 1986).

Freymuth, Bank, and Palmer (1984, 1985), and Freymuth, Bank, and Finaish (1985, 1986) used titanium tetrachloride as a smoke generating liquid for visualizing the flow over an airfoil. As air passed over the foil, smoke was released. The set-up was floodlit from above, and images were recorded by a high speed movie camera. These images showed the vortices generated around wings in great detail. The images also confirmed the Reynolds Number dependence of the vortex pattern in accelerating flow around airfoils, and the spanwise vortex structure in these flows. Fremuth et al's. (1986) most recent work dealt with the study of wing tip vortices in unsteady and steady flows. They described a wing tip vortex system that first occurred at Reynolds Numbers approaching 5200. This system consisted of leading and trailing edge vortices connected to each other at the front corner of the wing tip. More specifically, leading edge vortices were detected over and downstream of the surface of the wing. They appeared to end at the front corner of the wing. The main tip vortex had a conical shape with its apex pointing towards the front

corner of the wing tip. A trailing edge vortex sheet formed downstream on the foil. This trailing vortex was shown to decay into a series of discrete vortices visible as light vertical filaments. Many of these filaments were drawn into the main tip vortex. At present, they are continuing the study in order to determine the dependence of the tip vortex on foil profile, tip geometry, and aspect ratio.

Higuchi et al. (1985), Higuchi et al. (1986) made use of a Laser Doppler Velocimeter (LDV) system in their study of the vortex roll up process for an elliptically loaded wing, concentrating on Reynolds Numbers ranging from 50,000 to 500,000. The axial and tangential velocity measurements were used to demonstrate that the vortex core radius grew with increasing angle of attack, increasing downstream distance, and decreasing Reynolds Numbers. Their studies also included vortex circulation calculations. From these they determined that the total circulation was at most 45% of the theoretical mid span circulation at distances of even 4 chord lengths downstream of the foil. It was also found that the flow into the core did not necessarily originate at the tip, but could proceed at times from positions outside of the tip region, inward on the surface of the foil. They believed that the flow was affected by the boundary layers on both suction and pressure sides, which, in turn, were dependent on the angle of attack of the foil.

1.5 Experimental studies concerning tip vortex cavitation

Until recently, the number of studies that dealt expressly with tip vortex cavitation was very small. Although a few studies were conducted in the sixties, they were by no means comprehensive in regards to the scale of the problem that exists in pump and marine propeller usage. McCormick (1962) made one of the early studies. Perhaps the most important observation made during this study was that the vortex core radius depended strongly on the boundary layer that developed on the lifting surface. This observation has since been made quite often (see Higuchi et al. (1986) for example). Crimi (1970) conducted a study to determine the effect of sweep on hydrofoil loading and cavitation. His findings showed that as the sweep angle increased, the speed at which cavitation inception occurred also increased. Billet (1975) tested a series of rectangular hydrofoils, and found that the conditions for the onset of cavitation (and thus the pressure field) depended strongly on the Reynolds Number. Kuiper (1979) conducted an intensive study of the scale effects on propeller cavitation inception. His study showed that the radius where laminar separation starts was also a limit for the radial extent of cavitation. In addition, he found that if the boundary layer on the blades was tripped to a turbulent state, cavitation inception occurred when the estimated

local pressure reached the vapor pressure. Further investigation into cavitation on hydrofoils in turbulent flows was conducted by Murai et al. (1979). Their study also looked at the affects the boundary layer played in the inception, concentrating mainly on how the profile and changes in the angle of attack of the hydrofoil affected the boundary layer, and thus cavitation. These studies strongly depended on flow visualization images to back up the conclusions drawn. Additional studies were performed by Bosswell (1971) and Chandrashebhara (1976). Both concerned themselves with cavitation indices, both obtained results concerning cavitation inception conditions which agreed with those of Kuiper (1979) and Murai et al. (1979). Arakeri et al. (1982) expanded the study of tip vortex cavitation by including noise level measurements. Their findings showed that the noise level strongly depended on relationships drawn from the propeller's geometric configuration and operating characteristics. More specifically, the noise level depended on the axial velocity of the propeller, the rotational speed of the propeller, the pitch of the propeller, the diameter of the propeller, and the cavitation number encountered. Gostelow and Wong (1985) conducted a series of studies on impeller tip cavitation in axial flow pumps. Their study, which mainly involved photographic observations, confirmed the predominant role of the tip vortex in the cavitation behavior of the pumps.

A thorough study of tip vortex cavitation on elliptical foils was conducted by Higuchi et al. (1985, 1986) along with Arndt et al. (1985). They found that cavitation sound sources were localized to a region within one base chord length from the tip of the hydrofoil. This region corresponded to where the initial vortex roll up occurred. Additionally, they showed that the Rankine Vortex model was totally unacceptable as a predictive method to find the cavitation inception number. With this in mind, they attempted to develop their own model to predict the inception number, which also failed. At present, they are continuing the work in this area.

1.6 Studies covering means of alleviation and dissipation of the vortex

The severe problems associated with tip vortices motivated the development of various techniques for alleviating their effects and dissipating their strength. One technique consisted of modifying the load distribution on the wing in order to generate multiple vortices that dissipate each other (see Corsiglia et al. (1976)). Other techniques concentrated on the tip geometry and, as summarized by Platzer and Sounders (1979), included the addition of end plates, splines, bulbs, honeycombs, contravanes, winglets, porous tips, and the injection of liquid from ports located near the tip. Some radical measures, such as

a design in which propellers are mounted at the wing tips (as devised by Loth and Loth (1984)) have also been brought forward. Although all of these ideas have merit, most result in substantial losses in performance, and only a few are acceptable for use in cases where cavitation is a concern. Sounders and Platzer (1981) considered three techniques, namely the roughened or bulbous tip, a porous hydrofoil, and fluid injection near the tip. They found that all three methods resulted in a substantial reduction of cavitation inception indices. After evaluating the results, they concluded that the roughened tip was the most effective. Hallock and Eberle (1977) also discussed the various means for alleviation of the tip vortex. Their work suggests that dissipation schemes in use on airfoils are still inadequate since they fail to reduce the vortex's strength to a safe level.

Since these surveys have been published, others have continued to investigate alleviation methods. The effect of jet injection on the flow structure near a tip was studied photographically by Wu and Vakili (1984). They observed that, besides altering the entire pressure distribution, the jets caused the generation of several secondary vortex structures. Some of the vortices were parallel while others were perpendicular to the main flow. Childs (1986) conducted a numerical study of the lift augmentation via spanwise tip blowing, and showed that the tip vortex

was displaced outward and upward when blowing was used. This displacement caused an increased lift. Tavella (1985) conducted an experimental investigation of the subject of tip blowing. By injecting fluid at the tip of a wing, he was able to determine the effect that this blowing had on the tip vortex generated and the subsequent lift distribution of the foil. His results agree with Childs' (1986) numerical study, in that there was an increase in the effective span value, and an outward and upward displacement of the tip vortex. Eppler and Shen (1979), Shen and Eppler (1981), and Shen(1985)spent the past several years developing hydrofoils with optimized geometries. The design method they devised enabled them to decrease inception indices. In general, the new foils can perform under wider ranges of operating speeds than those currently used.

1.7 Rationale for the present investigation

As documented, there have been many studies performed which concern tip vortices. However, studies that deal with the development of the tip vortex in regions near the surface of the foil are limited in number and scope. This lack of interest is partially due to the fact that the aircraft related industries which sponsored the majority of the research projects were primarily interested in the wake behind a wing. In addition, the research efforts of the past were hampered by the inadequacies of flow

visualization techniques. Methods such as smoke injection (see Brashears and Hallock (1975)), wool tuft grids (see McCormick et al (1968)), and hydrogen bubbles (see Thompson (1975)), could only provide a gross and qualitative description of the flow structure. Surface-oil-flow studies (see Sounders and Platzer (1981)) were used to provide information about the flow phenomena close to the surface of the foil, namely the location of separation regions, reattachment regions, and transition (to turbulent flow) regions. However, being limited to the body surface, this method provided very little information about the vortex structure and its relation to the geometry and the boundary layer on the hydrofoil. More information is necessary in order to gain a deeper understanding of the tip vortex and the roll up process in the near field region where the onset of cavitation occurs. By obtaining a visual record of the vortex development as it progresses down the chord of the hydrofoil, it would be possible to determine the effect that such factors as Reynolds Number, incidence angle, chordwise position, and foil geometry have on the generation of the vortex and its roll up. The system could also be used to investigate the various secondary vortex structures that occur near the tip of the foil.

Obviously, there is a need to find a flow visualization technique capable of resolving the fine details of the vortex structure. A method is incorporated into the test

facility that captures these fine details. The technique selected involves generating a green (Argon-ion) laser sheet to slice the flow field at precise cross sectional locations and relies on laser induced fluorescence. As Rhodamine dye, which is distributed in the water, is exposed to the laser sheet, its fluorescing property makes intricate details of the flow structure at that cross section visible. The resulting images are unobstructed by the flow field outside of the sliced region. Several investigators, such as Dewey (1976), have used this method in the past.

There is an additional need to supplement the flow visualization images with accurate pressure distributions. Although pressure distributions over NACA-66 foil surfaces existed (see T. J. Mueller for example), they tend to include measurements taken only near mid-span positions. By placing pressure taps throughout the surface of the foil, (including a concentration of taps near the tip), it is possible to correlate the surface pressure distributions and the flow visualization studies. This correlation results in the documentation of the spanwise pressure gradients which are believed to generate the vortex roll up process, and the location of boundary layer separation regions. The results are also used to study the development of the tip vortex, and its effect on the surface pressure distribution near the tip.

CHAPTER 2 - APPARATUS AND TEST PROCEDURE

2.1 Flow visualization system

As discussed previously, a unique flow visualization system is necessary to allow the documentation of intricate details of the flow structure around the tip of the hydrofoil. To meet this requirement, a system that relies on laser induced fluorescence as the means of visualizing the flow (as developed by Dewey (1976)) is being used in the Purdue University Hydromechanics Laboratory Towing Tank. A description of the system is provided in section 2.4. Specifically, dye, which is introduced into the flow field, responds with spontaneous fluorescence as it enters the cross section illuminated by the laser sheet. This dye is almost invisible in unilluminated sections and as a result the recorded image is unobstructed by the flow outside of the sliced region. Care has to be taken during the design and implementation of such a system in order to insure that the laser and the illuminating optics will operate efficiently in the towing tank environment. It is also necessary to use an image recording method that is effective under the proposed test conditions.

A functional description of the flow visualization system is presented in figure II.1, further details are provided in figures II.2-II.3, a photograph of the test facility is presented in figure II.4, and an artist's sketch of the test facility is presented in figure II.5. The system consists of an eight watt Argon ion laser, a laser control device, an image recording camera, dye injection equipment, and a group of struts and optical components used for directing the beam and aligning the camera.

The eight watt argon ion laser is tuned with a prism to emit a three watt beam with a frequency of 514.5 nanometers. The laser and its controls are located inside a cooled, dust free, vibration isolated container. The output beam is directed by several mirrors into the illuminating foil, expanded into a thin sheet by a cylindrical lens, while its thickness is reduced to about 0.5 mm by a long focal length spherical lens. Rhodamine dye is introduced either by injecting it from ports located on the surface of the model, or by seeding the water in the tank shortly before each run. The image created by the dye in the illuminated sheet is focused by a series of lenses and recorded by a high resolution television camera. The magnification and resolution of the image is controlled by proper choice of lenses, and the details in each frame can be varied by changing the concentration of the dye. The

magnification can be changed so that the area shown on the screen of the television monitor ranges from (1 x 1) to (20 x 20) inches.

A special traversing system is designed for the flow visualization studies to allow for maximum flexibility in testing the hydrofoil. This setup consists of a main strut support that carries the model and two smaller struts. The first strut directs the illuminating laser beam while the second one contains the collecting optics that lead to the camera. All three components are shown schematically in figure II.1, the details of the main strut are displayed in figure II.2, and the smaller strut is presented in figure II.3. The model support can be traversed vertically and laterally. Once the proper location is reached, the entire system is rigidly locked in place. The structure is heavily supported and extremely rugged to minimize vibrations. The illuminating strut is located six inches from the wall of the towing tank and can be transversed axially (motionwise) so that any desired section on or behind the model can be illuminated. This strut has two overlapping sections, and its length could be changed by extending the inner section from the outer shell. The strut containing the periscope that leads to the camera usually trailed about ten feet behind the model. It also has two overlapping parts, and is mounted on a traversing system that allows motion both in the axial and lateral direction. The

axial movement of this periscope can be coupled with the illuminating foil by a lead screw in order to keep the illuminated section focused on the camera when the light sheet is shifted. This feature prevents the need to refocus the camera lens whenever the observed section is changed. The output from the television camera is observed on a stationary monitor and recorded on a high resolution video recorder. Images that appear in this thesis are 35 mm photographs taken off the screen of the monitor.

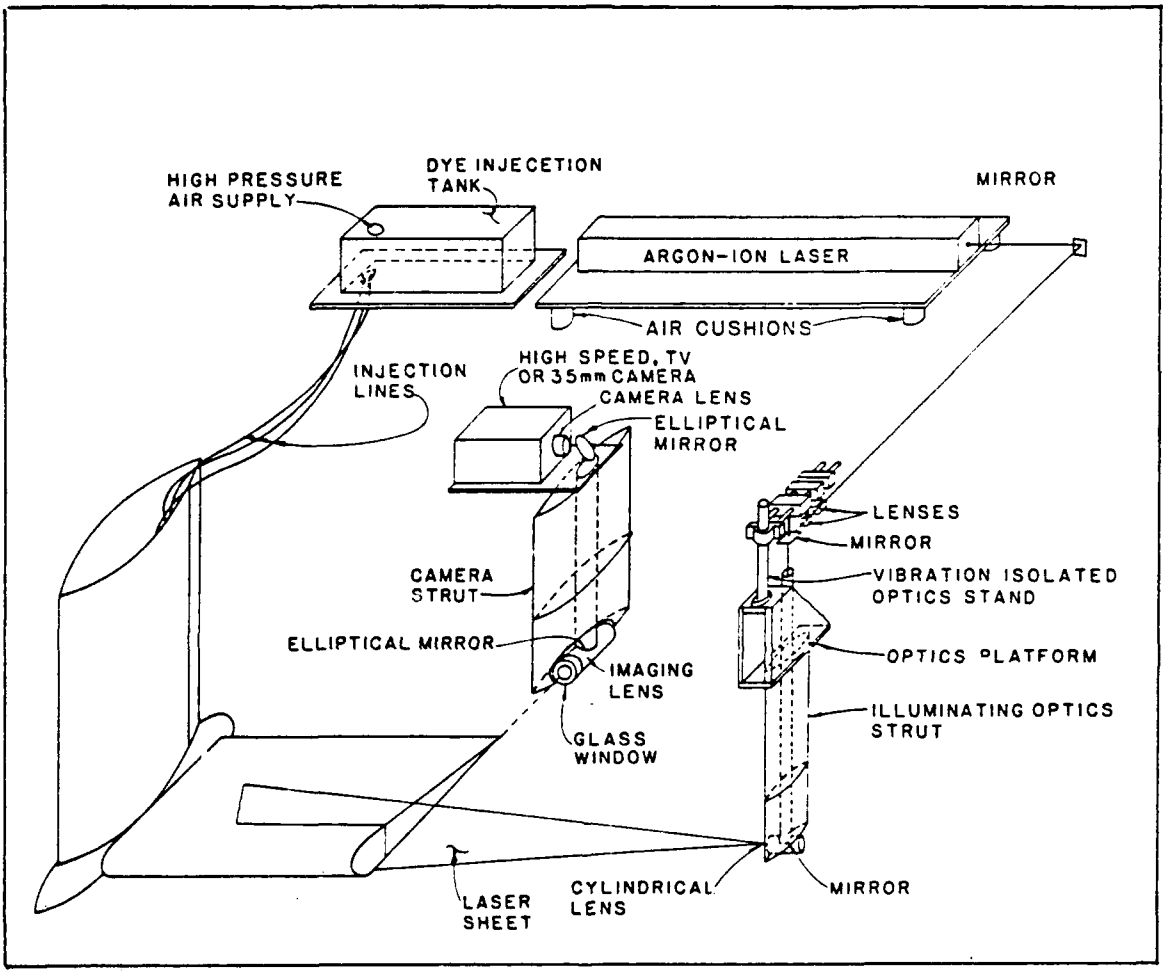

Figure II.1 A functional schematic of the flow visualization system.

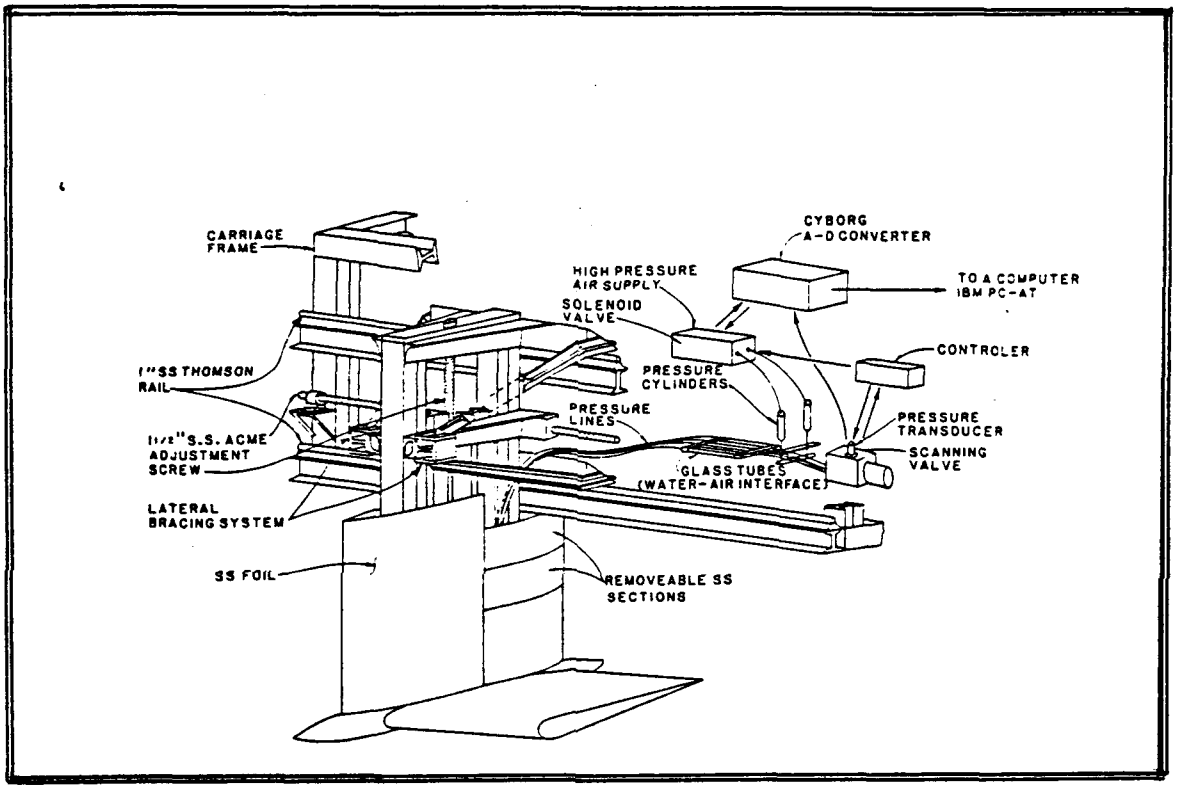

Figure II.2 A schematic description of the main transversing system and pressure measurement system.

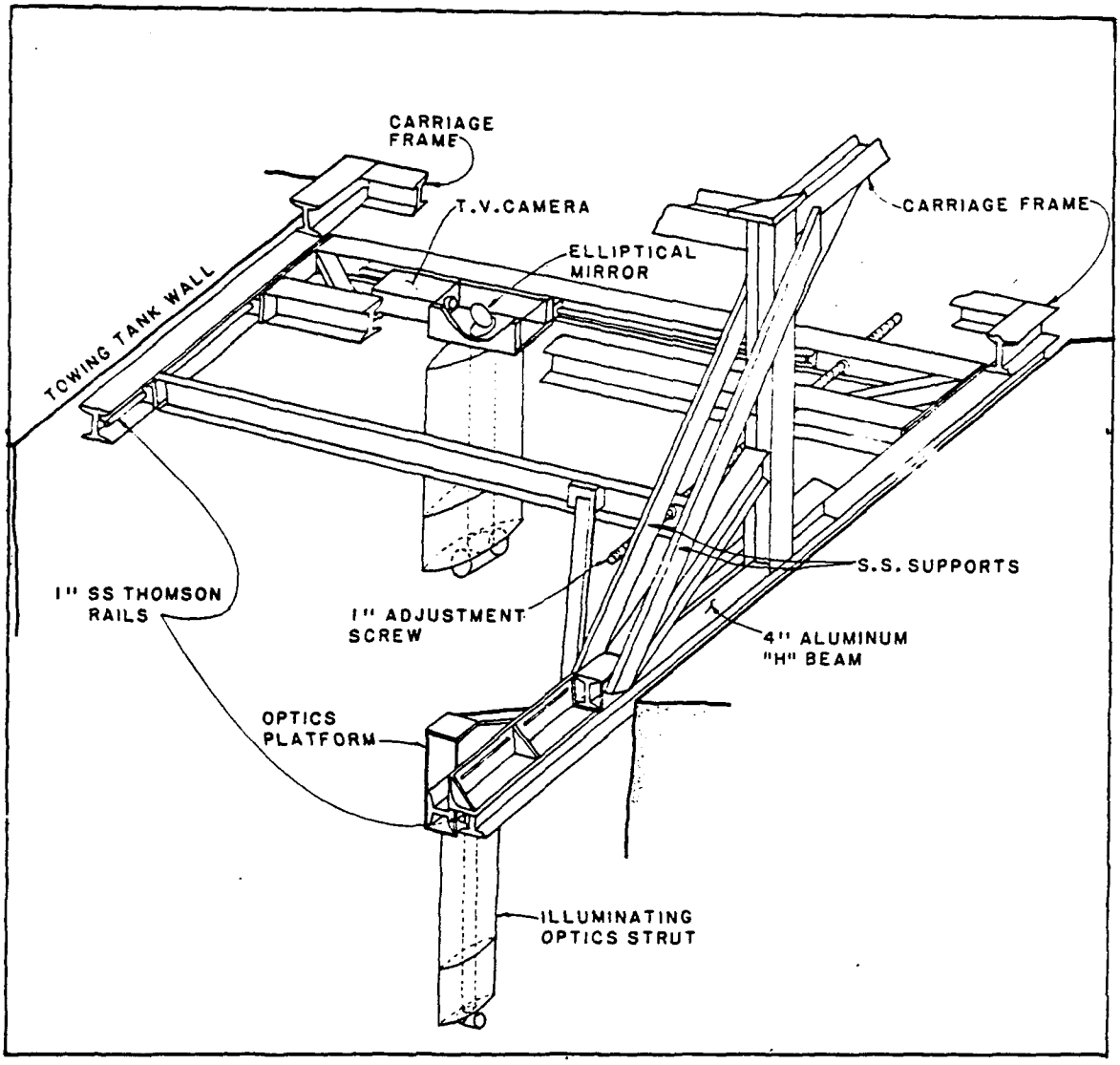

Figure II.3 A schematic description of the illuminating and collecting optics support mechanism.

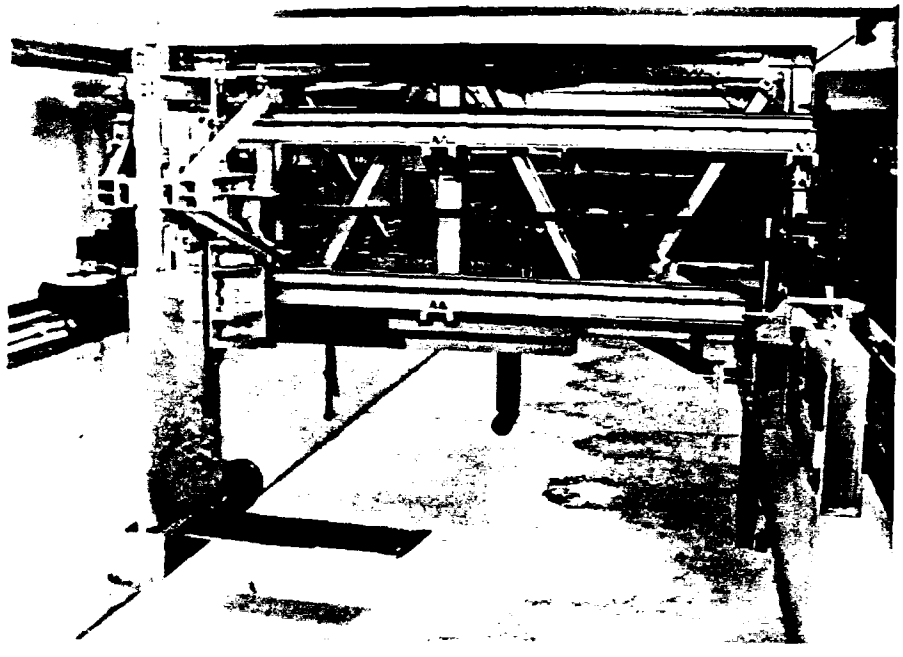

Figure II.4 A photograph of the towing tank test facility (with no water in the tank).

Figure II.5 An artist's sketch of the Purdue University Towing Tank. The numbered items are :

1. Laser Case
2. Pressure Measurement Case
3. Scanivalve Control Devices
4. Power and Signal Cables
5. Laser Coolant Pump
6. Mercury Manometer
7. Dye injection Tank
8. Cable Drive System
9. Rail Brush Mounts
10. Main Strut Support System
11. Main Strut
12. Hydrofoil
13. Laser Sheet
14. Illuminating Optics Support System
15. Illuminating Strut
16. Acrylic Window Panels
17. Pitot Tubes
18. "Cut-Out" View of the Camera Strut
19. Rails and Adjustable Mounting Plates
20. Illuminating Lamps

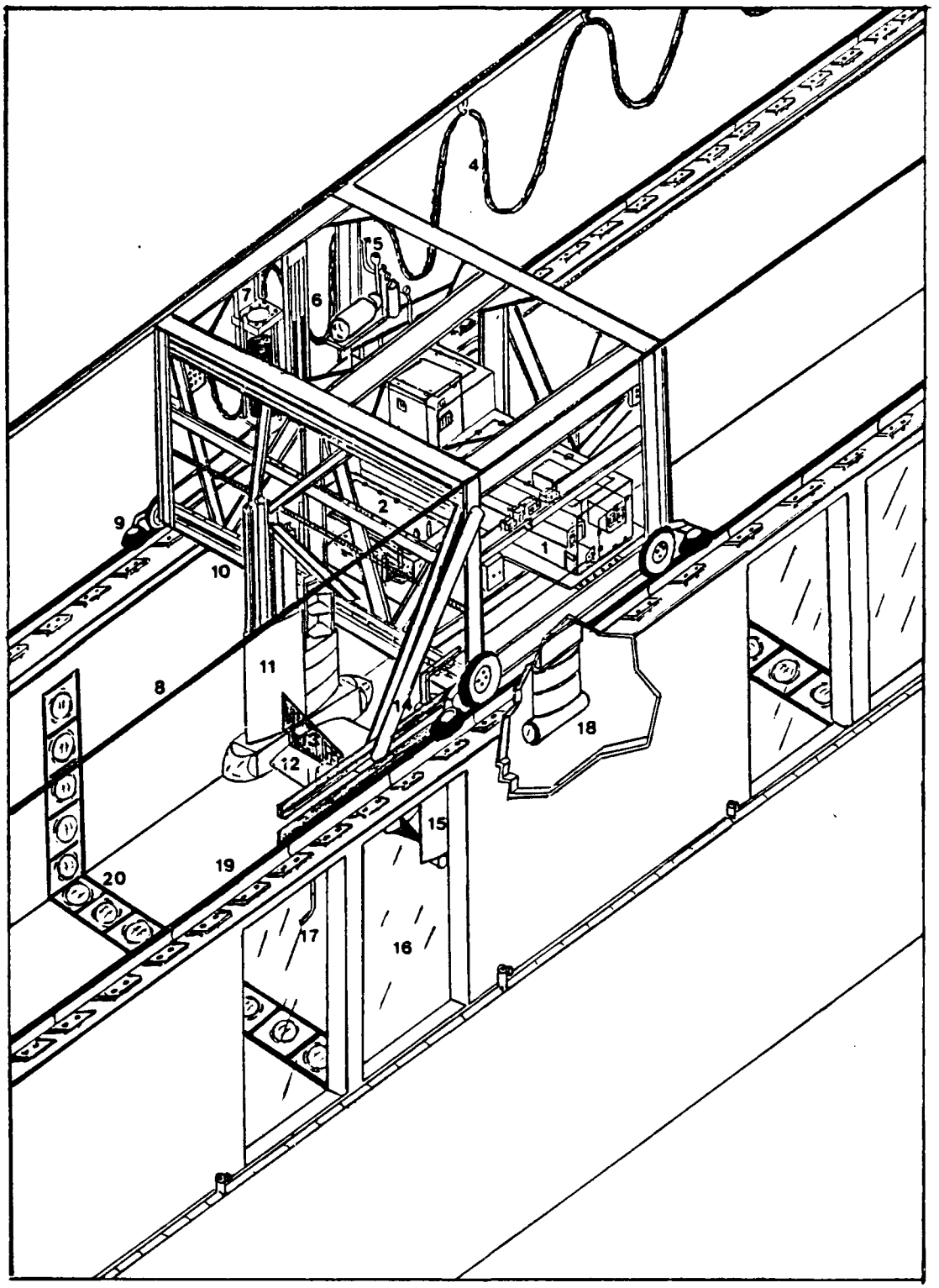

Figure II.5

2.2 Pressure measurement system

Figure II.2 also contains a description of the pressure measurement system to which the output of the surface taps are connected. A total of 270 pressure taps are distributed on the surface of the model, and their exact location is specified in figures B.1 and B.2 of appendix B. These taps are connected to plastic tubes which lead from the test body, through the inside of the main support strut, toward the carriage. There, each line is connected to a 1 ft. long horizontal capillary glass tube, which is positioned normal to the direction of carriage motion. An air-water interface is established inside these glass tubes whose purpose is described below. Plastic tubing connects the other end of the glass tubes to the cap of a scanning valve that contains a transducer. The control devices for the scanning valve are also mounted inside the carriage, and the output signal is routed through an analog to digital converter and stored in an IBM personal computer. The transducer is calibrated daily to insure that accurate measurements are taken.

Several problems associated with pressure measurements have to be overcome. The main concern is the slow scanning rate of the valve. It can scan only about 10 ports during a single towing tank run (at moderate to high speeds). A pneumatic control system and a pressure freezing

mechanism are employed to resolve this problem (as shown schematically in figure II.2). This system consists of a mechanism that freezes the pressure in the lines until the valve completes the entire cycle of its 48 ports. The mechanism includes a clamp, two gas cylinders, a solenoid valve that leads to a source of high pressure gas, and a control device. Before the towing tank carriage starts to slow down, an "electronic eye" activated the solenoid valve which directed the high pressure supply to the cylinders. The clamps then press the plastic tubes shut, freezing the pressure in the lines leading to the scanning valve. After the carriage is brought to rest, the valve is activated, and the output of the transducer is digitized and fed into a computer. When the scanning process is completed, the clamp is released and the system is ready for new measurements. This process requires the use of an air scanning valve, and the interface between air and water is kept at a constant elevation within the glass tubes.

Before each set of measurements, a suction device is used to draw water up through the pressure taps to a terminating location inside the horizontal glass tubes. The air-water interface that is created at that position is verified visually. Small sections of flexible tubing lead from the ends of the glass tubes to the connecting ports of

the scanivalve. The output from the transducer is then used to calculate the surface pressure distributions over the hydrofoil.

As noted before, repeated calibration of the pressure measurement system, including an estimate of the effect of clamping on the pressure inside the tubing, is performed daily. A mercury manometer and a small pressure chamber are installed inside the carriage for that purpose. Sources of errors in this setup are primarily the clamping mechanism and noise picked up by the long cables used in the system (special cable shielding and filtering of the signal are required). Estimated errors are in the 1 to 3 % range.

2.3 Test body

The foil chosen for use in the experiment is a NACA-66 series DTMB modified section with a 10 % thickness ratio and a 0.8 mean chamber line. Figure II.7 is a photograph of the resulting design, and a complete listing of the profile geometry is given in table A.1 of appendix A. The model has a rectangular planform with a 2 ft. chord and a 3 ft. semispan. It is composed of six attached sections, three upper, three lower, and is made of aluminum.

There are several factors that have to be considered regarding the design and manufacture of the hydrofoil. Among these are: the attachment to the supporting strut, incidence angle variations and control, accommodations for the pressure measurement lines and dye injection ports, cost considerations, corrosion protection, and foil profile accuracy.

The attachment device is designed to provide a sturdy (vibration limiting) mount for the hydrofoil. It consists of a solid steel block which is attached to the main strut of the carriage. The block has a hole through which a 2 inch diameter stainless steel screw is inserted. This screw is used to set and then lock the system once the incidence angle of the hydrofoil is fixed. As shown in Figure II.6, the model is attached to the strut by connecting two circular stainless steel plates. The first is

welded to the mounting block and the second to the supporting bars of the hydrofoil. Each of these plates have a series of holes through which pins are inserted which enable fixing the incidence angle between -15 and +15 degrees at 1 degree increments. The support mechanism is located inside a 10 inch diameter and 36 inch long cylindrical fuselage with an ogive nose (see figure II.6). The foil is also reinforced by two (1.5 x 1.5) inch stainless steel bars which extend out from the root towards the tip. Calculations show that for bars of this thickness, deflection due to expected lift is negligible.

In order to accommodate 270 pressure tubes, the foil is hollow (see figure II.7). Aluminum tubes machined flush with the surface of the foil are laced through the interior of the foil and terminate at its root. The plastic tubes which lead to the pressure measurement system are attached to the terminated ends of the aluminum tubes.

To hold down costs and ease construction, an N-C milling process is used to machine the profile of the foil (see figure II.8). The mill has a 2 ft. travel limitation in the x direction, and a 1 ft. travel limitation in the y direction. By entering the profile coordinate data into the machine, and considering the compensation required for cutter radius, it is possible to generate the hydrofoil shape.

Finally, to guard against corrosion, an electrolys nickel process is used to place a protective coating over the surface of the foil. Additionally, a "metal to metal" connection is established between the foil and magnesium cylinders that are placed on the floor of the towing tank. These cylinders act as sacrificial anodes to eliminate the corrosion process on the aluminum test body.

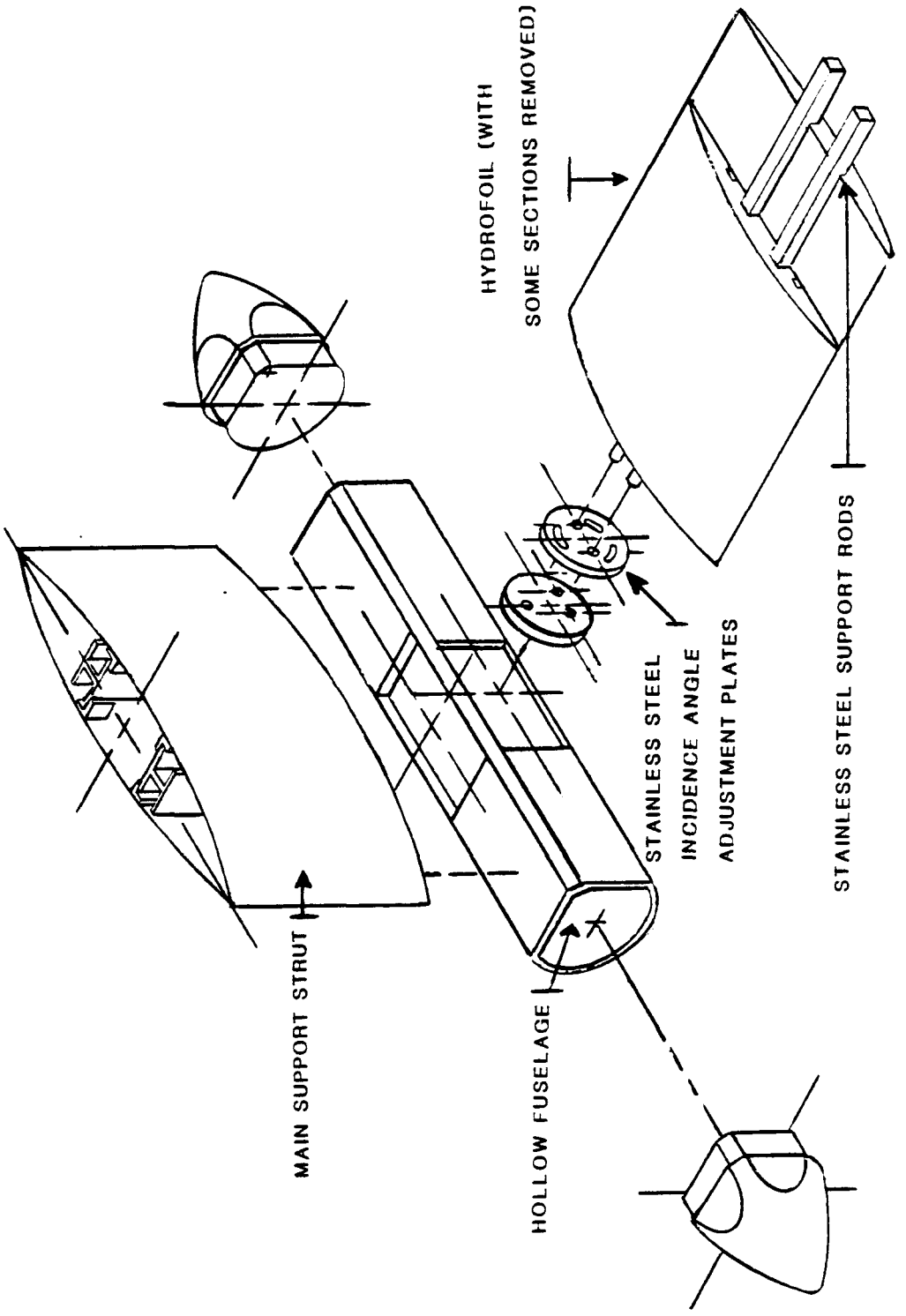

Figure II.6 A three dimensional drawing of the hydrofoil and mounting system.

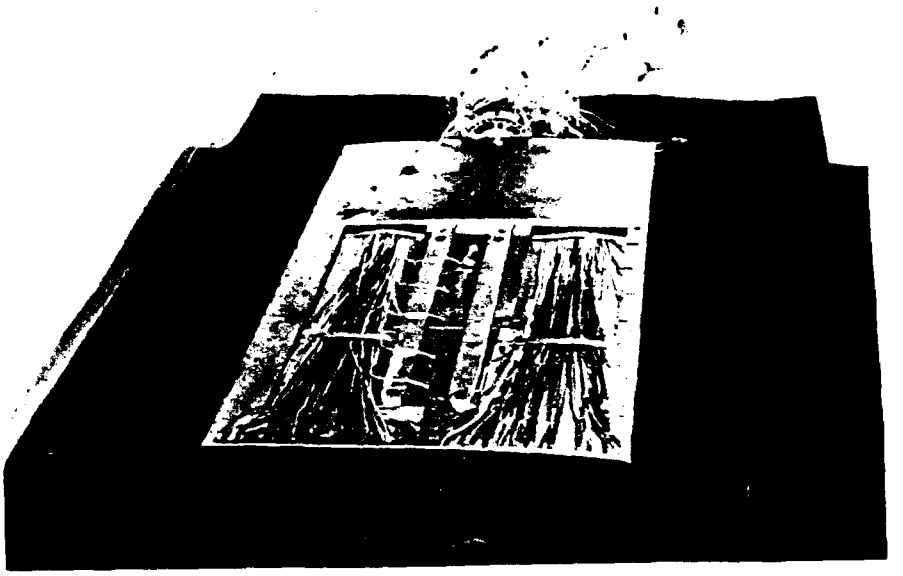

Figure II.7 A photograph of the hydrofoil with its bottom cover removed.

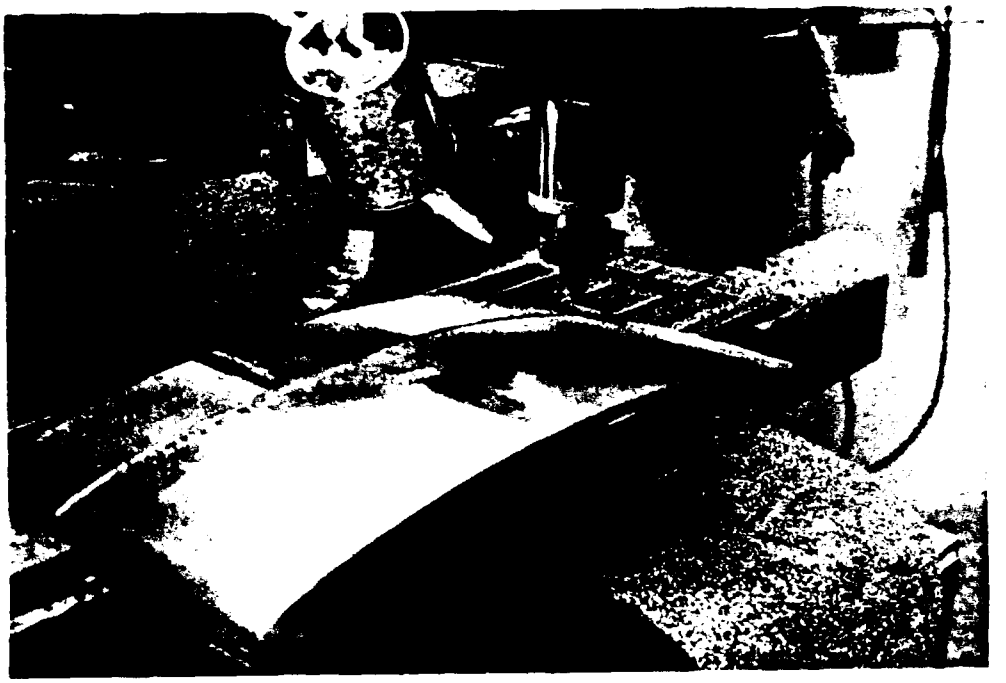

Figure II.8 A photograph of the hydrofoil during the N-C milling process.

2.4 Towing tank test facility

The towing tank test facility is located in the Purdue University Civil Engineering Hydromechanics Laboratory. A sketch of the test facility is presented in figure II.5. The tank itself is 156 ft. (47.5 m.) long, 11 ft. (3.4 m.) wide, and 5 ft. (1.5 m.) deep. It is equipped with a towing carriage which houses an array of flow visualization and pressure measuring devices. The carriage is connected through a gear box to a 50 H.P. D.C. motor. The power provided enables the carriage to reach a speed approaching 15 ft./sec. (4 m./sec.). At this maximum speed, the usable towing length with uniform velocity is approximately 100 ft. (30 m.). Acrylic window panels are located in two sections along the side wall of the tank. Submerged lamps are positioned adjacent to these windows to aid visualization. The water in the facility is constantly filtered, taking about two days to cycle the entire volume through the system. Chlorination is provided through a device which is attached to the filter. Draining and filling the tank is accomplished through the use of the pumping system housed in the laboratory.

CHAPTER 3 - FLOW VISUALIZATION RESULTS

3.1 Introduction

The trends observed while analyzing the flow visualization records are documented in this section. This analysis is performed by using the unique playback unit of the video recorder which allows freezing individual frames without losing resolution. This feature enables measuring the tip vortex size and location directly off the television monitor. Photographs (such as those shown in this chapter) are taken using a 35 mm camera focused directly on the frozen image projected on the screen.

Four dimensions are measured off the video records. A sketch describing these terms is given in figure III.1. The first term, D, is the characteristic vortex size (from this point on it will be referred to as the vortex diameter, although it is not the actual diameter of the vortex core) which is defined as the inner oval portion visible in each image (as sketched in figure III.1). The second term, LZ, denotes the horizontal distance between the vortex center and the tip of the hydrofoil. The third term, LY, denotes the vertical distance between the surface of

the wing and the center of the vortex. The fourth term, LS, denotes the horizontal distance between the tip of the wing and the attachment line located on the surface of the hydrofoil. Definitions of the chordwise dimension terms, X and C, which are used to designate the cross sectional location of the vortex, are also given in Figure III.1 Appendix D gives an explanation of the uncertainty encountered in the flow visualization data measurements.

3.2 Changes with increasing chordwise position

Figures III.2 and III.3 are photographs that demonstrate the growth of the vortex as it progresses down the chord length of the foil. A graphic representation of this trend is given in figure III.8. It can be seen, for example, that at a 12 degree incidence angle and velocity of 1.0 ft./sec., the diameter of the vortex, D, increases from D/C = 0.028 to 0.067 and to 0.074 as the chordwise position increases from X/C = 0.50 to 0.75 and to 0.80, respectively. Similarly, at 5 degrees and 1.0 ft./sec., D/C increases from 0.011 to 0.038 and to 0.050 as X/C increases from 0.5, to 0.75, and to 0.80, respectively. This trend is evident at higher speeds also. For example, at 5 ft./sec. and an angle of 8 degrees, D/C increases from 0.012 to 0.030 and to 0.064 as X/C increases from 0.50, to 0.70, and to 1.00, respectively. It is interesting to note

that in many cases, this growth rate approaches a linear relationship.

Figures III.9 and III.10 are graphs which demonstrate that the vortex center line shifts as the chordwise position increases. For example, figure III.9 shows that at a velocity of 1.0 ft./sec., the horizontal location of the vortex center, LZ, moves inward (toward the root of the foil) from LZ/C = 0.027 to 0.042 and to 0.053 at 8 degrees and from 0.013 to 0.027 and to 0.040 at 5 degrees as X/C increases from 0.50 , to 0.70, and to 1.00, respectively. The vertical location of the vortex center, LY, rises from LY/C = 0.017 to 0.024 and to 0.048 at 8 degrees and from 0.004 to 0.015 and to 0.035 at 5 degrees as X/C increases from 0.50 to 0.70 and to 1.00, respectively.

Figure III.11 clearly demonstrates that the horizontal location of the attachment line, LS, moves inward as the chordwise position increases. For example, at an angle of 8 degrees and a velocity of 1 ft./sec., LS/C moves toward the root of the foil from 0.061 to 0.167 as X/C increases from 0.50 to 1.00.

It is obvious that there is some correlation between the growth rate of the vortex and its center line shift. However, it should be noted that their rates of change are different. A doubling in vortex size would not necessarily mean that its center line will experience a shift of the

same magnitude. For example, at an angle of 12 degrees and a velocity of 1 ft./sec., the diameter, D , increases 100 % (from D/C = 0.028 to 0.056) as X/C increases from 0.50 to 0.70. At the same conditions, the horizontal location of the tip vortex center, LZ, increases only by 21 % (from LZ/C = 0.038 to 0.046) and the vertical location of the tip vortex center, LY, increases by 9 % (from LY/C = 0.021 to 0.023).

3.3 Changes with increasing velocity

Velocity (and therefore the Reynolds Number) also has a role in determining vortex growth and location. Figures III.4 and III.5 are photographs that demonstrate the tendency of the diameter to decrease with increasing velocity. This trend is also shown graphically in figure III.8. In this figure, the trend is clearer at higher incidence angles. For example, at an incidence angle of 8 degrees and X/C = 1.0, D/C decreases from 0.075 to 0.063 as the velocity increases from 1 ft./sec. to 5 ft./sec. respectively. At a 5 degree incidence and X/C = 0.90, D/C decreases from 0.057 to 0.039 as the velocity increases from 1 ft./sec. to 5 ft./sec.

Increasing the velocity also results in an outward shift of the vortex center line, as seen in figures III.9 and III.10. Again, the trend is clearer at higher incidence

angles. For example, at an incidence angle of 8 degrees and X/C = 1.0, LZ/C decreases from 0.053 to 0.032 as the velocity increases from 1.0 ft./sec. to 5.0 ft./sec. In addition, figure III.10 shows that LY/C decreases from 0.048 to 0.042 as the velocity increases. Again, the rate of decrease experienced by LZ/C, LY/C, and D/C values are related, but are not identical.

Figure III.11 shows that the location of the attachment line moves outward (toward the tip of the wing) as the velocity increases. For example, at an angle of 8 degrees and X/C = 1.0, LS/C decreases from 0.167 to 0.125 as the velocity increases from 1 ft./sec. to 5 ft./sec..

3.4 Changes with increasing incidence angle

The photographs in figure III.6 show that the vortex increases in size as the incidence angle of the foil increases. This trend is also shown graphically in figure III.8. From figure III.8, at X/C = 0.8 and a velocity of 1.0 ft/sec., D/C increases from 0.050 to 0.074 as the angle changes from 5 to 12 degrees. Similarly, at a speed of 5 ft./sec., D/C increases from 0.030 to 0.047 as the angle changes from 5 to 12 degrees.

The vortex center line tends to show an inward and upward shift as the angle increases. For example, figure III.9 shows that at X/C = 0.8 and a velocity of 1.0

ft./sec., LZ/C increases from 0.034 to 0.048 as the angle increases from 5 to 12 degrees. Under these conditions, figure III.10 shows that LY/C increases from 0.018 to 0.029. Similarly, figures III.9 and III.10 show that at a speed of 5 ft./sec, LZ/C increases from 0.034 to 0.046, and LY/C increases from 0.016 to 0.028 as the angle increases from 5 to 12 degrees.

The horizontal location of the attachment line increases as the angle increases as shown in figure III.11. For example, at a velocity of 3 ft./sec. and at X/C = 1.0, LS/C increases from 0.081 to 0.125 as the angle changes from 2 to 8 degrees.

These trends, and the knowledge that the incidence angle affects the dimensions and extent of the laminar separation zone on the hydrofoil (particularly at higher angles of incidence), suggest that the vertical distance between the vortex center and the surface is related to boundary layer separation. This conclusion has already been postulated by Higuchi et al. (1986)

Changing the angle of attack has a stronger affect (in regards to location shifts and size changes) than variations in velocity (see figures III.8, III.9, III.10, and III.11). Therefore, it appears that the amount of liquid flowing into the tip vortex is highly dependent on the

angle of attack. This observation agrees with Arndt et al's. (1985) findings.

3.5 Secondary structures

Secondary vortex structures are visible throughout the flow visualization images. It seems that the geometry of the foil has a role in their formation. Figure III.7 contains photographs of the phenomena commonly encountered, which include counter-rotating vortices and shear layer eddies.

Counter-rotating vortices are visible in the majority of flow visualization images. A counter-rotating vortex, shown in figure III.7 (a), figure III.2 (a), and figure III.3 (a), first appears in regions to the left of the tip vortex, in upstream locations on the foil. This secondary structure seems to wrap around the main vortex in a clockwise direction as it progresses down the chord. Finally, as the trailing edge is approached, this structure appears in regions to the right of the tip vortex. It is interesting to note that this secondary structure seems to be larger than the main tip vortex at upstream regions and low incidence angles (0 and 2 degrees). This puzzling phenomenon is an addition to peculiar trends observed during other studies with foils having the same profile. For

example, Mueller (1986) measured negative lift values on a NACA-66 foil at an incidence angle of 1 degree.

In addition to counter-rotating vortices, shear layer eddies (as shown by figures III.7 b,c,d) are clearly seen in many of the images. These eddies are visible mainly at lower speeds in regions near the tip of the foil. The slow recording rate of the video camera hinders their detection at higher velocities. These eddies travel from the base of the wing, up the edge of the tip, and become entrained in the main tip vortex. It appears that the tip shape has an important role in determining the structure and behavior of these eddies. Other models with different tip shapes should be tested to verify this statement.

3.6 A discussion of the flow visualization results

3.6.1 The Reynolds Number's affect on cavitation

The size reduction of the vortex with increasing velocities has a major impact on the conditions for the onset of tip vortex cavitation. The pressure in the core of a Rankine Vortex , P_c, can be expressed by

$$P_c - P_\infty = \frac{\rho \Gamma^2}{8 \pi^2 r_c^2} \quad , \qquad 3.1$$

where r_c is the radius of the core, ρ is the liquid density, Γ is the circulation, and P_∞ is the pressure at infinity, Γ of a wing can be directly related to the lift coefficient, C_L, by

$$\Gamma \propto \frac{1}{2} V C C_L \quad , \tag{3.2}$$

where C is the chord length. The equal sign is replaced by a proportionality relationship since the tip vortex is not fully developed and as a result some of the wing circulation is still outside the main vortex (see El-Ramey and Rainbird (1977)). Thus:

$$C_{pc} = \frac{P_c - P_\infty}{\frac{1}{2} \rho V^2} \propto - \frac{C^2 C_L^2}{16\pi^2 r_c^2} \quad . \tag{3.3}$$

If we assume that the onset of cavitation occurs when P_c is equal to the vapor pressure, P_v, then the cavitation inception index, σ_i, defined by

$$\sigma_i = \frac{P_{\infty i} - P_v}{\frac{1}{2}\rho V^2} \quad , \tag{3.4}$$

is related to the pressure coefficient, C_{pc}, by

$$\sigma_i + C_{pc} = \frac{P_c - P_v}{\frac{1}{2} \rho V^2} = 0 \quad . \tag{3.5}$$

Or, by substituting the result from eq. 3.3 in eq. 3.5,

$$\sigma_i \propto \frac{C^2 C_L^2}{r_c^2} \quad . \tag{3.6}$$

Thus, a reduction in the radius of the core results in an increase in the values of σ_i.

3.6.2 The incidence angle's affect on the vortex size

It is clear that the incidence angle has a major impact in determining the size of the tip vortex. This can be shown mathmatically. Firstly, the lift experienced by the foil can be expressed as

$$L = \frac{1}{2} \rho V^2 C C_L \quad , \qquad 3.7$$

where ρ is the liquid density, S is the span length, V is the free stream velocity, C is the chord length, and C_L is the lift coefficient. The lift coefficient is directly proportional to the incidence angle by

$$C_L = K \alpha \quad , \qquad 3.8$$

where K is an arbitrary constant, and α is the incidence angle. Circulation can be defined as

$$\Gamma = 2 V_\theta \pi r_c \quad , \qquad 3.9$$

where V_θ is the vortex's axial velocity component. Substituting eq. 3.2 into eq. 3.9

$$r_c \propto \left[\frac{C}{4 \pi} \frac{V}{V_\theta} K \right] \alpha \qquad 3.10$$

The terms inside the parenthesis approach a constant value in certain Reynolds Number ranges and axial positions.

When this occurs, eq. 3.10 shows that the size of the tip vortex is only a function of the incidence angle.

3.7 Empirical equations

The data found in figures III.8, III.9, and III.10 may be presented as empirical relationships. The resulting equations are functions of three parameters; the Reynolds Number, the incidence angle, and the chordwise position of the tip vortex. The series of experiments performed on the hydrofoil are conducted within the following parameter ranges: a Reynolds number ,(Re_c), of 10^5 to 5×10^6 , an incidence angle, (α), of 0 to 12 degrees, and a chordwise location, (X/C), of 0.48 to 1.00. The equations are designed to give acceptable estimates of the vortex size and location when the the operating parameters of the foil are within the above ranges. The equation for (D/C) is developed to be in the form of:

$$D/C = F(X/C,\alpha)G(X/C,Re_c) \quad .$$

From boundary layer analysis, it is evident (assuming that D is somehow related to the boundary layer) that the Reynolds Number should be raised to a power close to 0.5 for a laminar boundary layer and other powers for a turbulent boundary layer. Growth with the incidence angle was expected to be in the form of eq. 3.10. As will be shown shortly, this is not the case in the present results.

3.7.1 Tip vortex diameter

The empirical expression developed for the tip vortex diameter (defined in figure III.1) is as follows:

$$D/C = F(X/C,\alpha,Re_c)=G(\alpha,X/C)H(Re_c,X/C) \qquad 3.7$$

where:

$$G(\alpha,X/C)=0.0378(X/C)\{2.1-2(\alpha+1)^{-0.5}(X/C)^{-1}\}$$

$$H(Re_c,X/C)=\{0.75+1.45*10^{3}(X/C)^{0.6}(Re_c)^{-0.6}\} \quad .$$

A plot comparing measured values of the tip vortex diameter and those calculated by equation 3.7 is presented in figure III.12

Equation 3.7 is divided into two parts. The first one ,G, is a function of the chordwise position and the incidence angle. The second one, H, is a function of the chordwise position and the Reynolds Number. As is evident from these equations, once the incidence angle and the chordwise position are fixed, the diameter is proportional to $Re_c^{-0.6}$. Similarly, once the velocity and location are fixed, the vortex size is inversely proportional to the square root of the incidence angle.

Most importantly, the ability to condense the experimental data to this empirical relationship is remarkable. By looking at figure III.12, it is clear that the data scatter is relatively low. This scatter is higher near the

upper region of the graph (for values which correspond to low speed conditions) than the lower region (for values which correspond to high speed conditions). The standard deviation of the empirical data is +/- 0.003, which can serve as the error margin.

3.7.2 Tip vortex center: horizontal location

The empirical expression for the horizontal location of the tip vortex center line (defined in figure III.1) is as follows:

$$LZ/C = J(X/C,\alpha,Re_c)=\{K(\alpha,X/C)L(Re_c,X/C)\}^{0.9} \qquad 3.8$$

where:

$$K(\alpha,X/C)=0.0295(X/C)\{0.28(\alpha+1)^{0.6}-0.25\}$$

$$L(Re_c,X/C)=\{0.75+1.74*10^{3}(X/C)^{0.6}(Re_c)^{-0.6}\} \quad .$$

A plot comparing measured values of the horizontal location of the tip vortex center to those calculated by equation 3.8 is presented in figure III.13

Equation 3.8 is also divided into two parts. The first, K, is a function of chordwise position and incidence angle, the second, L, is a function of chordwise position and Reynolds Number. The results show that once the angle and chordwise position are fixed, the horizontal location is proportional to $(Re_c^{-0.6})^{0.9}$. Similarly , once the

Reynolds Number and chordwise position are fixed, the horizontal location is proportional to $((\alpha+1)^{0.6})^{0.9}$.

Again, the agreement between the equation and the data is remarkable. From the results in Figure III.13, it is evident that the scatter is small. The data scatter increases as the upper range is approached (which corresponds to lower velocity readings). Also, this scatter is greater than that found for the the results of equation 3.7. Here, the standard deviation is +/- 0.004.

3.7.3 Tip vortex center: vertical location

The empirical expression for the vertical location of the tip vortex center line (defined in figure III.1) is as follows:

$$LY/C = N(X/C,\alpha,Re_c) = Q(\alpha,X/C)P(Re_c,X/C) \qquad 3.9$$

where:

$$Q(\alpha,X/C)=0.0231\{0.35(\alpha+1)(X/C)^{1.1}-0.22\}/(\alpha+1)^{0.5}$$

$$P(Re_c,X/C)=\{0.75+13.6(X/C)^{0.6}(Re_c)^{-0.2}\} \quad .$$

A plot comparing measured values of the vertical location of the tip vortex center to those calculated by equation 3.9 is presented in figure III.14

Again, the equation is divided into two parts. The first one, Q, is a function of the chordwise position and

the incidence angle, the second one, P, is a function of the chordwise position and the Reynolds Number. The equations show that the Reynolds Number is not as great a factor in determining the vertical location of the tip vortex center as it is in determining the horizontal location. Here, once the incidence angle and the chordwise position are fixed, the vertical location of the tip vortex center is proportional to $Re_c^{-0.2}$. Similarly, once the chordwise position and the Reynolds Number are fixed, the vertical location is proportional to the square root of the incidence angle.

The agreement between this equation and the data is also fairly good. Besides the upper region of the graph (at low velocities) , the scatter appears to be relatively uniform, and the standard deviation is +/- 0.003.

3.7.4 Conclusion

In conclusion, it should be reemphasized that these formulae are empirical equations developed to match data gathered under specific test conditions. Further studies are necessary to predict the affect that geometry and boundary layer changes have on the location and size of the tip vortex.

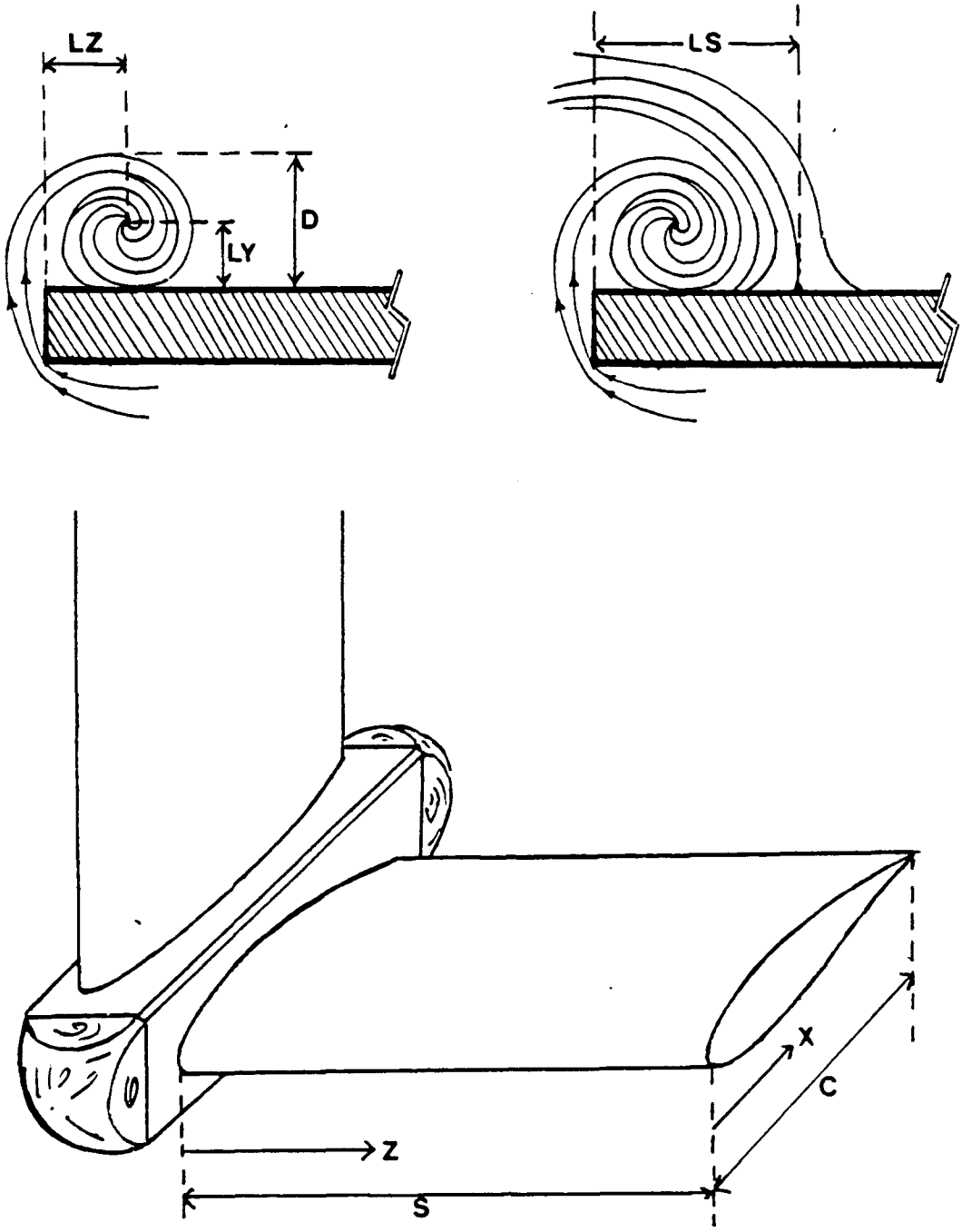

Figure III.1 Sketches illustrating D, LZ, LY, LS, X, Z, C, S, used in the present study.

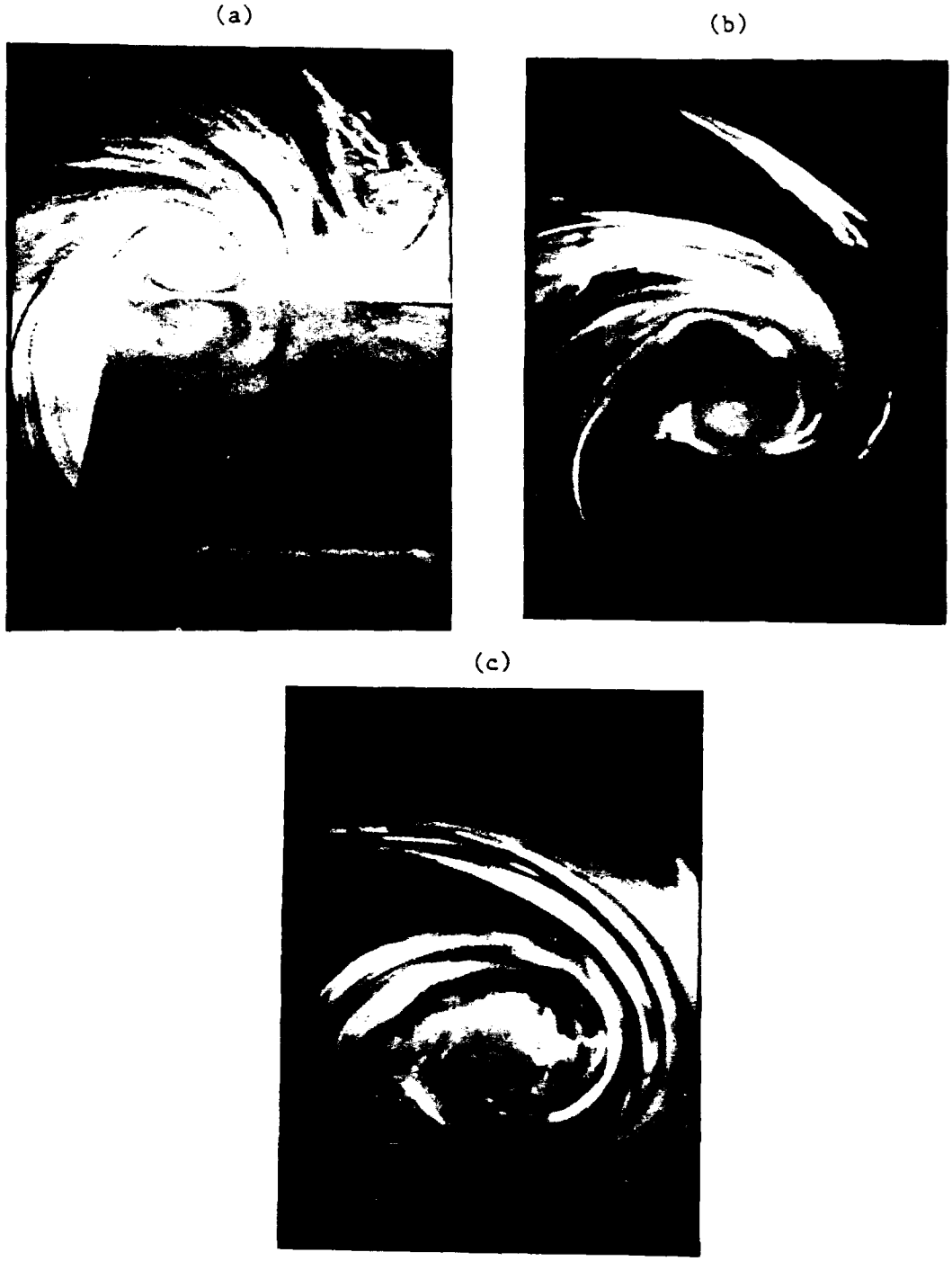

Figure III.2 A sequence of photographs demonstrating the development of a tip vortex as the chordwise position increased.
$\alpha = 5^{o}$, v = 1.5 ft./sec.
(a) X/C = 0.69 (b) X/C = 0.92 (c) X/C = 1.02

Figure III.3 A sequence of photographs demonstrating the development of a tip vortex as the chordwise position increased.
$\alpha = 5^{o}$, v = 1.0 ft./sec.
(a) X/C = 0.69 (b) X/C = 0.82
(c) X/C = 0.92 (d) X/C = 1.00

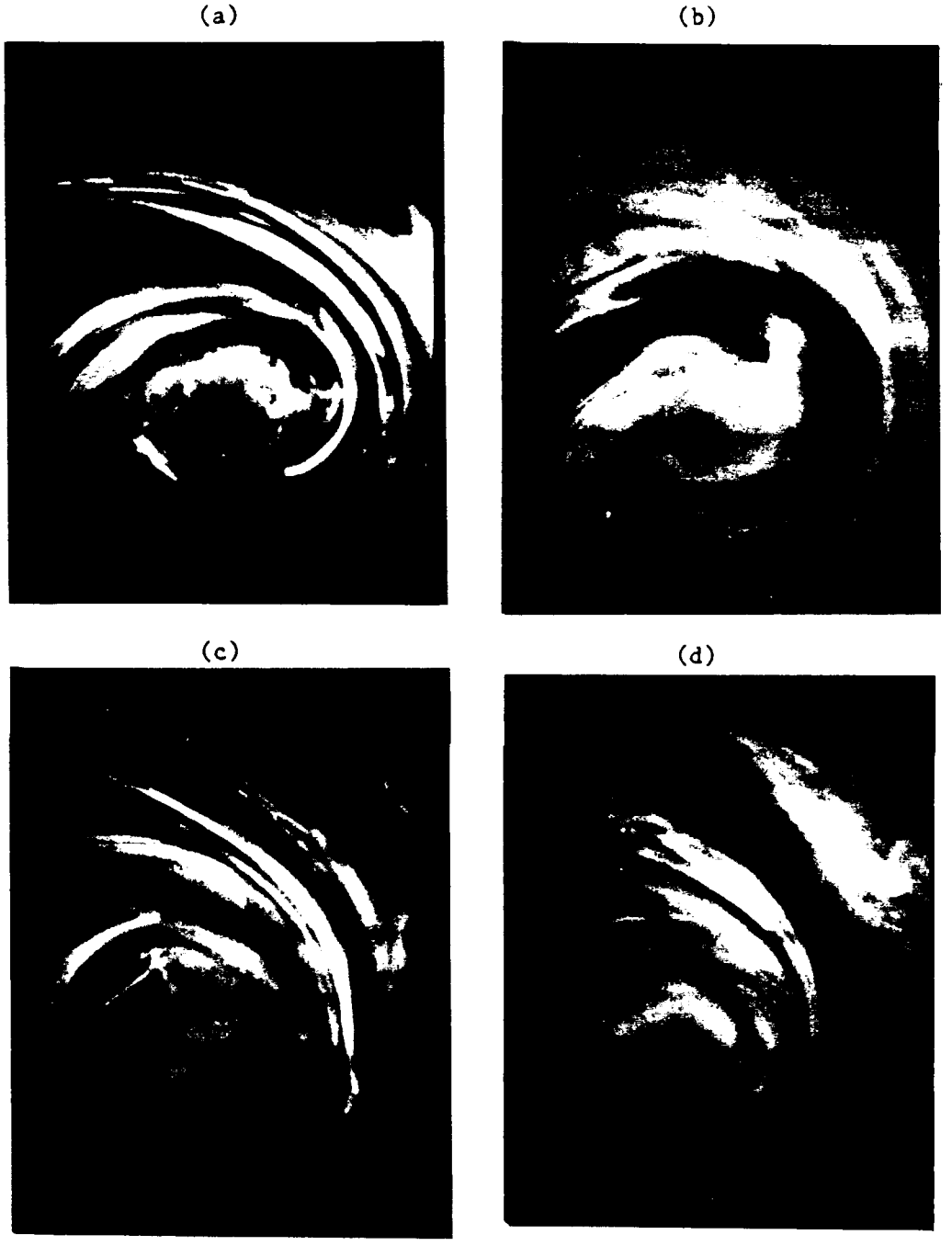

Figure III.4 A sequence of photographs demonstrating the dependence of the vortex size on the free stream velocity just downstream of the trailing edge.
$\alpha = 5^{o}$
(a) V = 1.5 ft./sec. (b) V = 3.0 ft./sec.
(c) V = 6.0 ft./sec. (d) V = 8.0 ft./sec.

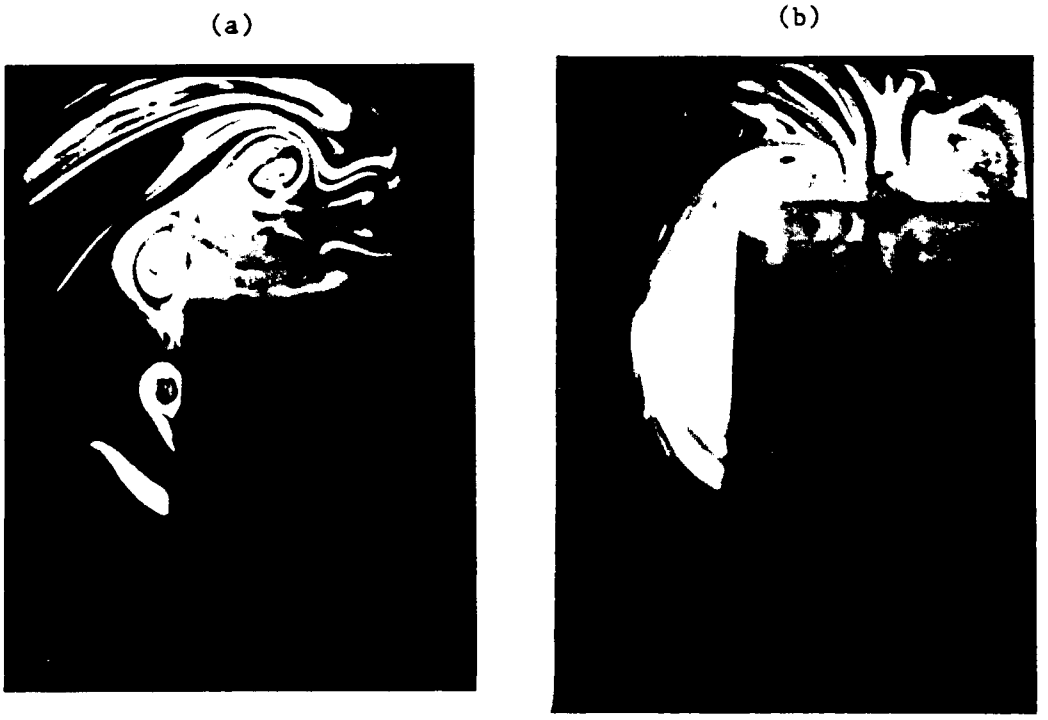

Figure III.5 A sequence of photographs demonstrating the dependence of the vortex size on the free stream velocity.
X/C = 0.46, $\alpha = 8^{o}$
(a) V = 0.2 ft./sec. (b) V = 1.5 ft./sec.

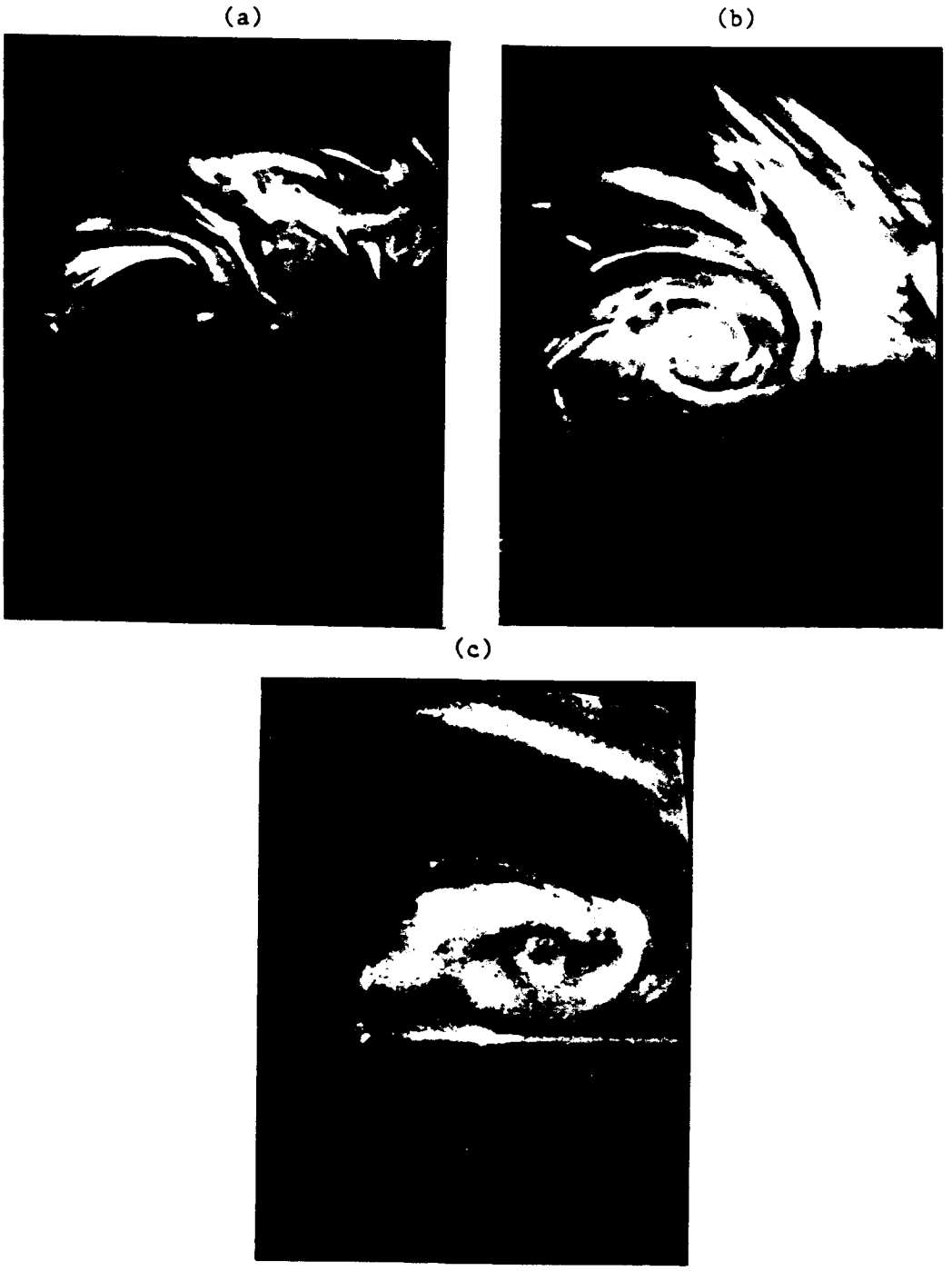

Figure III.6 A sequence of photographs demonstrating the dependence of the vortex size on the incidence angle.
V = 2.6 ft./sec., X/C = 0.82
(a) $\alpha = 2^{o}$ (b) $\alpha = 5^{o}$ (c) $\alpha = 12^{o}$

Figure III.7 A series of photographs showing primary and secondary flow structures.

(a) V = 1.5 ft./sec., $\alpha = 2^{o}$, X/C = 0.70
(b) V = 0.4 ft./sec., $\alpha = 5^{o}$, X/C = 0.92
(c) V = .15 ft./sec., $\alpha = 12^{o}$, X/C = 0.46
(d) V = .15 ft./sec., $\alpha = 12^{o}$, X/C = 0.46

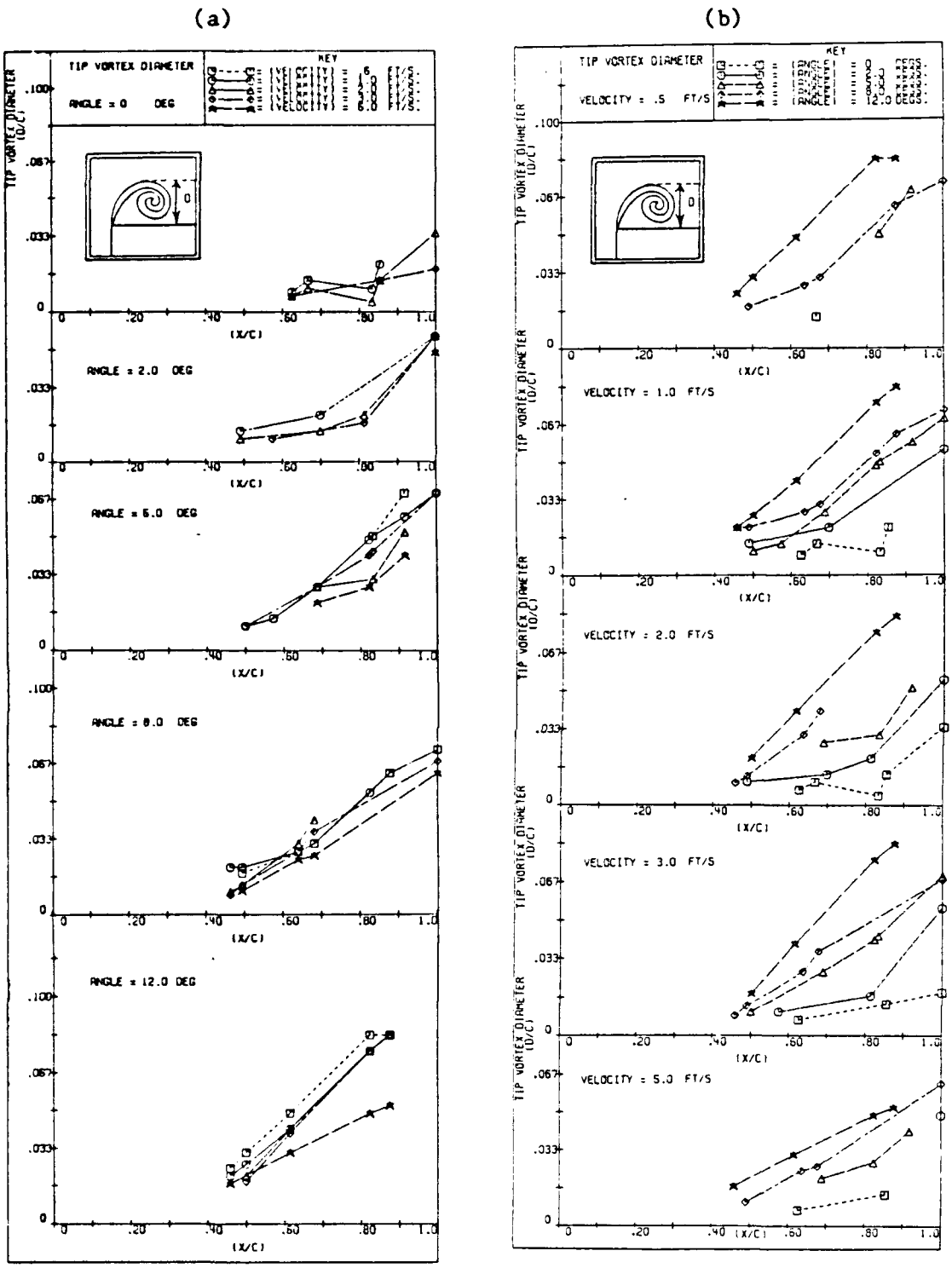

Figure III.8 Tip vortex size as measured from the flow visualization images.
(a) The angle is fixed, the velocity is varied
(b) The velocity is fixed, the angle is varied

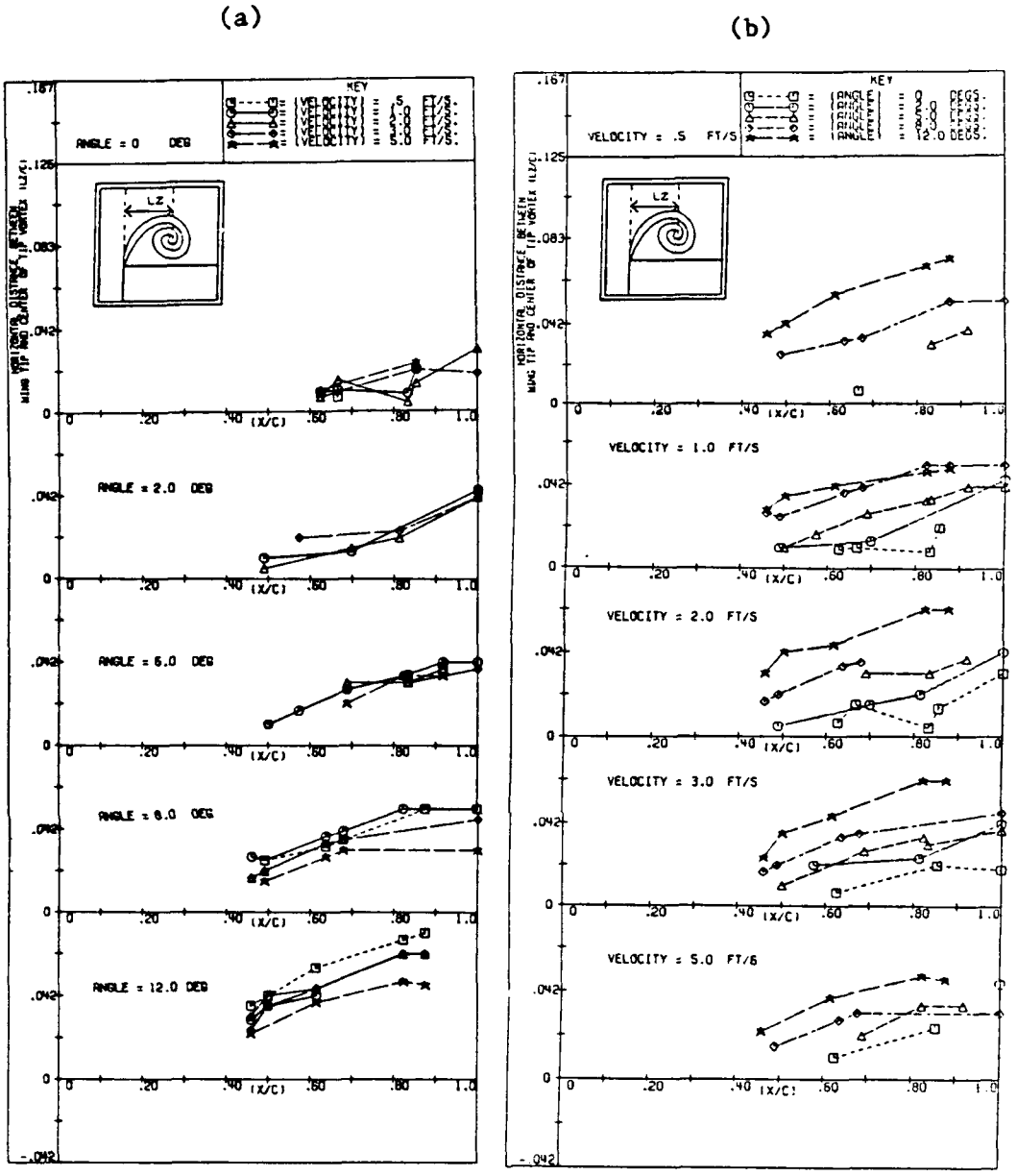

Figure III.9 The horizontal location of the tip vortex center as measured from the flow visualization images.
(a) The angle is fixed, the velocity is varied
(b) The velocity is fixed, the angle is varied

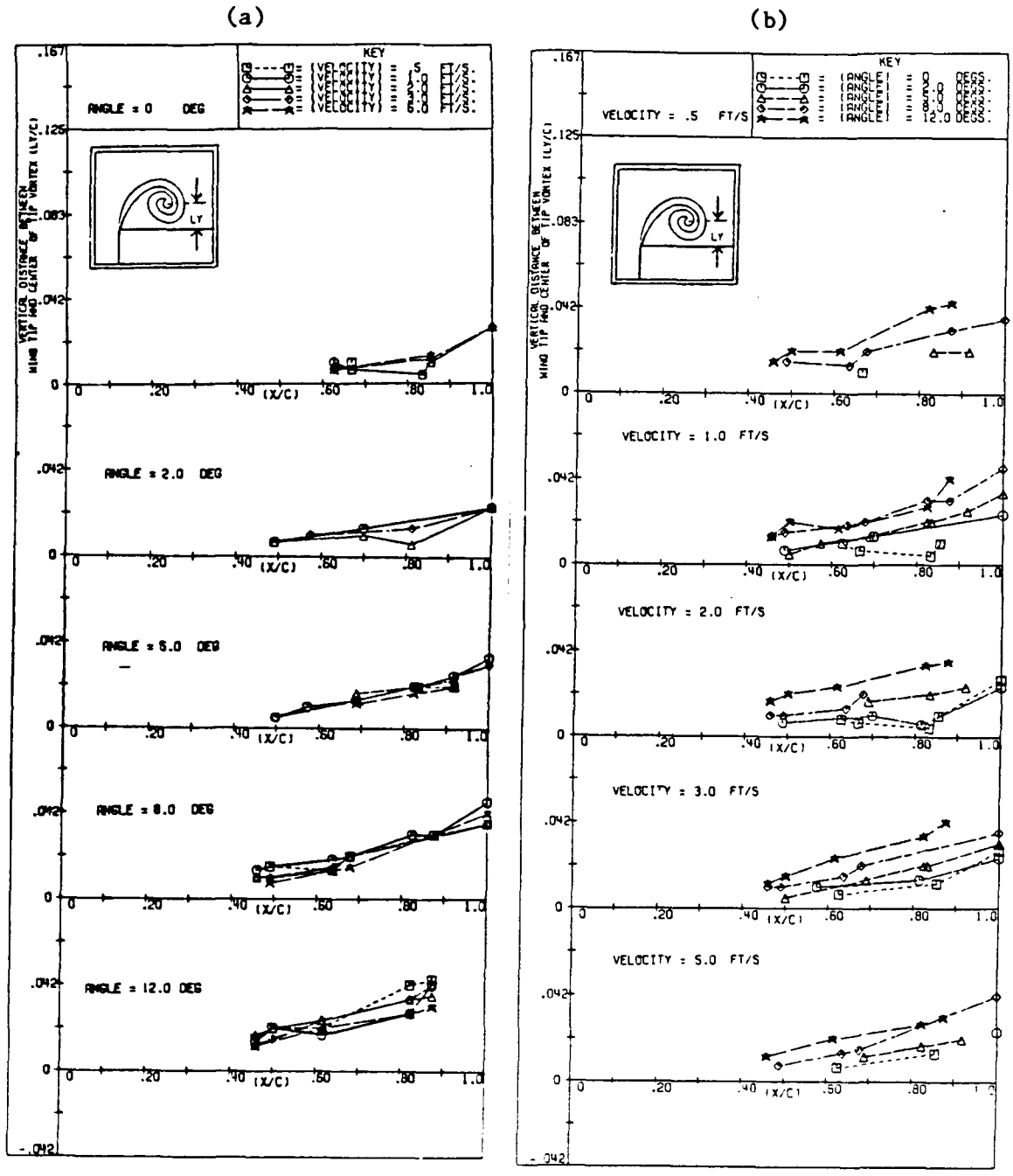

Figure III.10 The vertical location of the tip vortex center as measured from the flow visualization images.
(a) The angle is fixed, the velocity is varied
(b) The velocity is fixed, the angle is varied

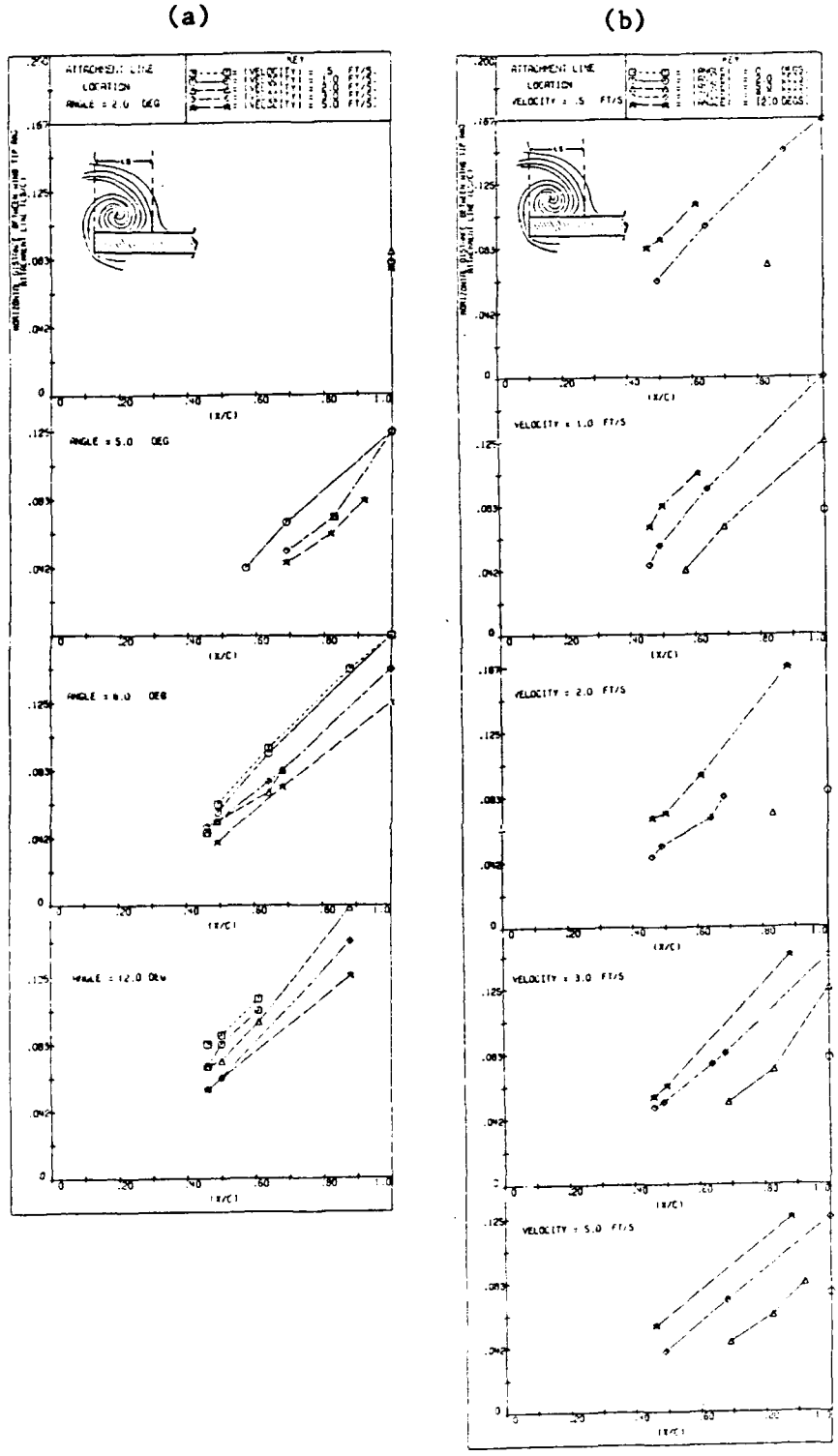

Figure III.11 The location of the attachment line as measured from the flow visualization images. (LS is defined in figure III.1)
(a) The angle is fixed, the velocity is varied
(b) The velocity is fixed, the angle is varied

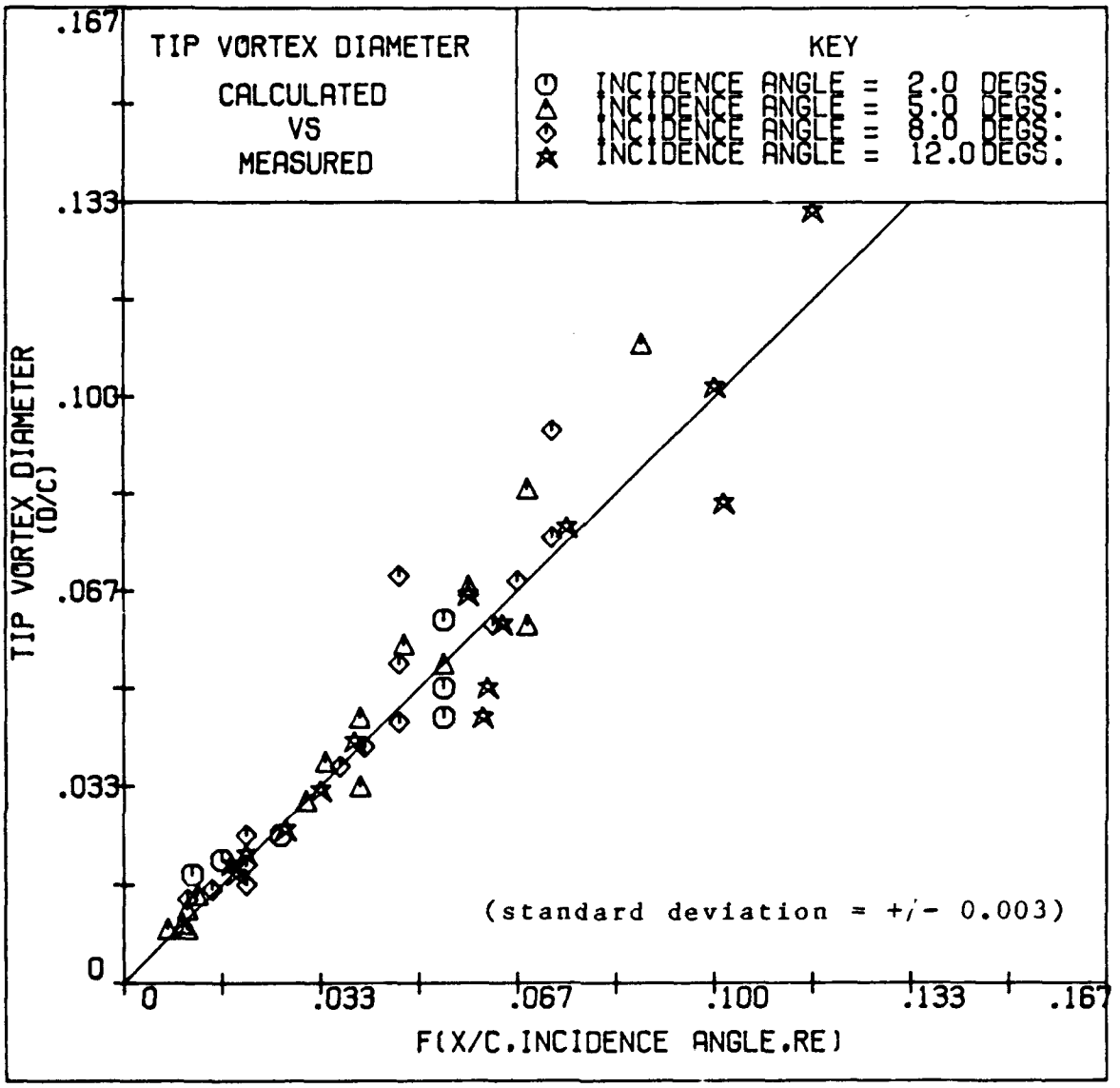

Figure III.12 A comparison between the empirical expression for the tip vortex diameter and the measured results. Where:

$$D/C = F(X/C,\alpha,Re_c)=G(\alpha,X/C)H(Re_c,X/C)$$

$$G(\alpha,X/C)=0.0378(X/C)\{2.1-2(\alpha+1)^{-0.5}(X/C)^{-1}\}$$

$$H(Re_c,X/C)=\{0.75+1.45*10^{3}(X/C)^{0.6}(Re_c)^{-0.6}\}$$

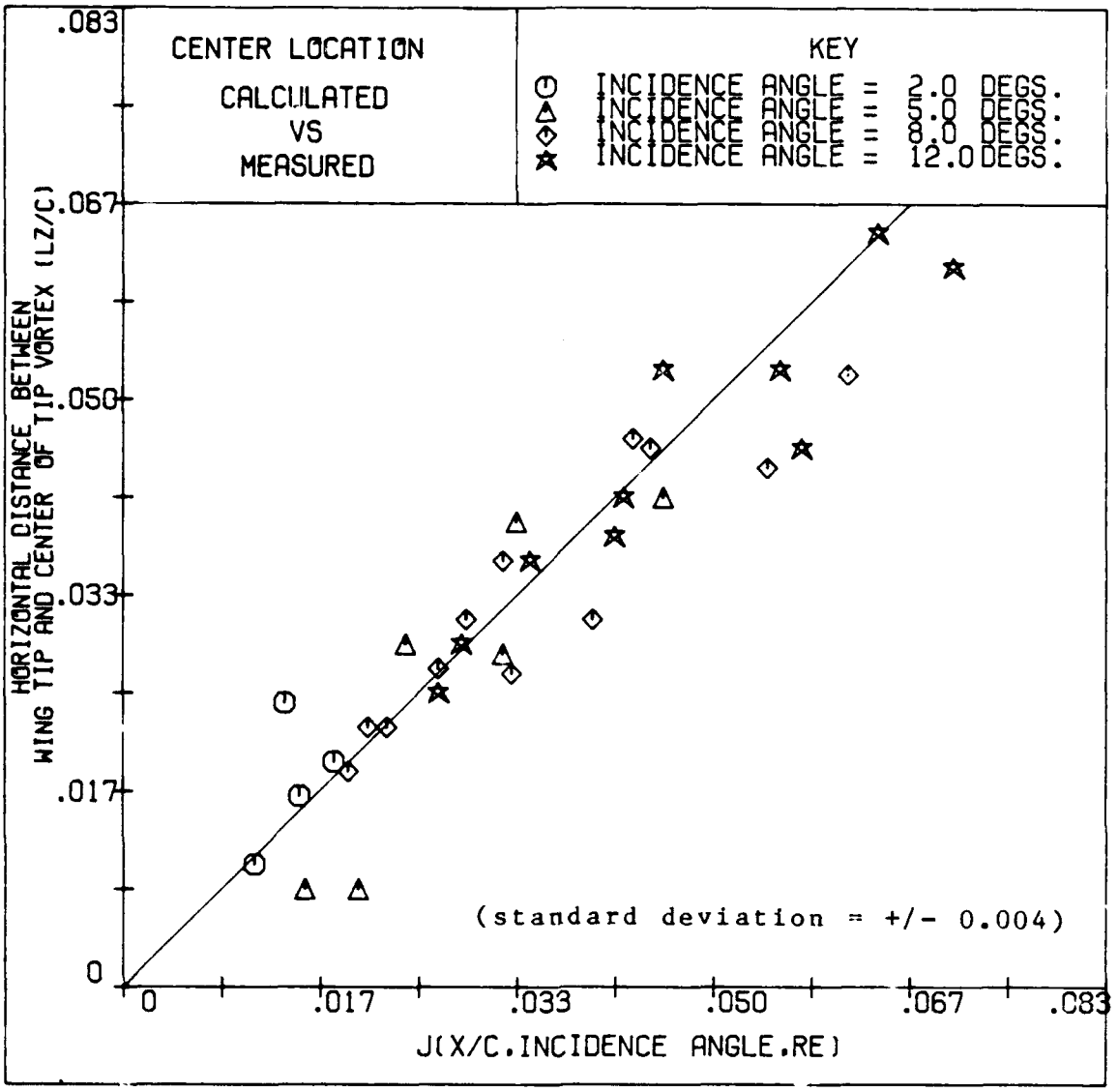

Figure III.13 A comparison between the empirical expression for the horizontal location of the tip vortex center and the measured results. Where:

$$LZ/C = J(X/C,\alpha,Re_c)=\{K(\alpha,X/C)L(Re_c,X/C)\}^{0.9}$$

$$K(\alpha,X/C)=0.0295(X/C)\{0.28(\alpha+1)^{0.6}-0.25\}$$

$$L(Re_c,X/C)=\{0.75+1.74*10^{3}(X/C)^{0.6}(Re_c)^{-0.6}\}$$

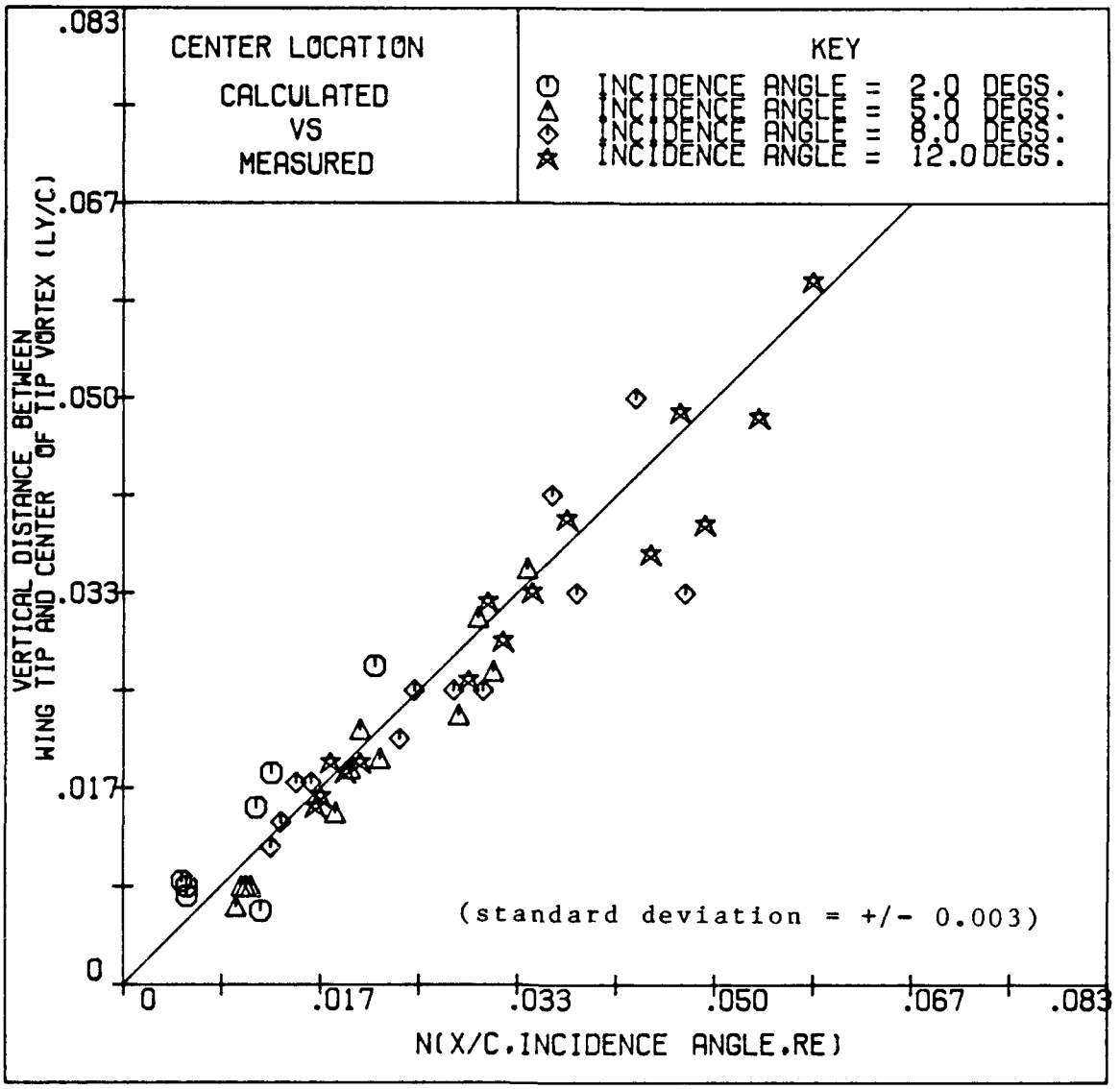

Figure III.14 A comparison between the empirical expression for the vertical location of the tip vortex center and the measured results. Where:

$$LY/C = N(X/C,\alpha,Re_c) = Q(\alpha,X/C)P(Re_c,X/C)$$

$$Q(\alpha,X/C)=0.0231\{0.35(\alpha+1)(X/C)^{1.1}-0.22\}/(\alpha+1)^{0.5}$$

$$P(Re_c,X/C)=\{0.75+13.6(X/C)^{0.6}(Re_c)^{-0.2}\}$$

CHAPTER 4 - PRESSURE MEASUREMENT DIAGNOSTICS

4.1 Introduction

The following chapter summarizes the results of surface pressure measurements. Some of the results are surprising at first, but after careful examination, it is possible to correlate the distributions with the results of the flow visualization experiments. This comparison leads to a greater understanding of the interaction between the flow structure near the surface of the foil and the resulting pressure distribution.

The various parameters used in this section are displayed in figure III.1. Included are the chordwise dimensions, X and C, and spanwise dimensions, Z and S. The results are presented by using the surface pressure coefficient term, C_p, defined as follows :

$$C_p = \frac{P - P_\infty}{\frac{1}{2} \rho V^2} \quad . \tag{4.1}$$

Here, P is the local pressure, P_∞ is the pressure at infinity, ρ is the fluid's density, and V is the free stream velocity.

4.2 Spanwise pressure distributions

Spanwise distributions of the surface pressure coefficients are presented in figure IV.1. The test velocity is set at 5 ft./sec., and the incidence angle ranges from 0 to 12 degrees.

Several trends can be identified from these graphs. First, a gradual increase in the pressure coefficient is clearly visible as the tip region on the upper surface of the hydrofoil is approached (See figure IV.1). At an angle of 5 degrees and chordwise position of 0.40, the coefficient of pressure increases from -0.63 to -0.40 as the spanwise location increases (toward the tip) from 0.64 to 0.82 (as seen from figure IV.1.) Similarly, at X/C = 0.60, C_p increases from -0.56 to -0.40 as Z/S increases from 0.64 to 0.82. As the incidence angle increases to 8 degrees, the gradient becomes more pronounced. For example, at a chordwise position of 0.40, the value of the pressure coefficient increases from -0.77 to -0.56 as the spanwise location increases from 0.64 to 0.82 (figure IV.1).

As expected, the gradients decrease in strength as the chordwise position increases beyond the minimum pressure region. For example, at an angle of 8 degrees and a chordwise position of 0.60, the pressure coefficient rises from -0.60 to -0.52 as the spanwise location increases from 0.64 to 0.82. Close to the trailing edge, (for example at

X/C = 0.85), the pressure coefficient no longer shows any spanwise increase. Instead, it remains at a level of C_p = -0.28 in the range of Z/S = 0.64 to 0.82.

To recapitulate, these results document the strong spanwise pressure gradient that exists on the surface of the foil. They show that this gradient increases with increasing incidence angle and is more pronounced near the minimum pressure zone. Past researchers have argued the fact that the volume of fluid entrained in the tip vortex is related to the spanwise fluid flow on the surface of the foil, and thus, to lateral pressure gradients (see Freymuth et al. (1986) for example). Since this spanwise flow is a function of the incidence angle and chordwise location, the vortex size must also be a function of these parameters. This observation agrees with those drawn from the flow visualization results of chapter 3.

The spanwise distributions also show evidence of the vortex structures located near the tip of the foil. The occurrance of counter-rotating secondary structures (as documented in the photographs of figures III.7) can be seen in the spanwise pressure distributions developed for 0 and 2 degree incidence angles. The structures appear as pronounced dips in the value of the pressure coefficient at spanwise locations near Z/S = 0.90. For example, at an angle of 2 degrees, Z/S = 0.89, and X/C = 0.05 and 0.40,

the coefficient of pressure drops to -0.80 and -0.90, respectively (figure IV.1). At an angle of 0 degrees, a spanwise location of 0.85, and chordwise locations of 0.20 and 0.60, the coefficient of pressure drops to -0.76 and -0.84, respectively. At angles greater than 2 degrees, the dip associated with these secondary structures disappears. This fact is not surprising, due to the increased influence of the main tip vortex on the pressure distributions as the incidence angle of the foil increases.

The tip vortex is also evident in the spanwise distribution graphs. The dip associated with this vortex is clear in every plot. It occurs in spanwise locations ranging from 0.95 to 0.99. For example, in figure IV.1, at an angle of 2 degrees, a spanwise location of 0.99, and chordwise positions of 0.60 and 0.85, the coefficient of pressure drops to -0.36 and -0.64, respectively. Similarly, at an angle of 8 degrees, spanwise locations of 0.99 and 0.97, and chordwise positions of 0.60 and 0.85, the coefficient of pressure drops to -0.80 and -1.10, respectively. These examples highlight the fact that the pressure dip moves in a spanwise direction toward the root of the foil as its chordwise position increases. The spanwise distributions also show that the pressure drops to its lowest value near the tip of the wing at downstream locations. For example, at an 8 degree incidence angle, the minimum pressure coefficient is -1.10 and occurs at X/C =

0.85, and Z/S = 0.97. Similarly, at 12 degrees, the minimum pressure coefficient is -1.80 and occurs at X/C = 0.85 and Z/S = 0.99.

Variations with the incidence angle are also evident from the results. By comparing the values of C_p at 5^o and 8^o, at a spanwise location of 0.99, and a chordwise position of 0.60,the pressure coefficient drops from -0.32 to -0.80, respectively. These trends agree with conclusions drawn from the flow visualization images (as discussed in chapter 3). They suggest that the dimensions and strength of the tip vortex increases and its center location moves inward (toward the foil's root section) as the chordwise location and the incidence angle increases.

4.3 Chordwise pressure distributions

Figures IV.2 and IV.3 present chordwise pressure distributions for the hydrofoil at various angles of attack. The distributions in Figure IV.3 are taken on the pressure side of the foil. Those in Figure IV.2 are taken on the suction side of the foil. The distributions taken on the suction side of the foil display several important trends. Focusing first on the regions near the tip, at incidence angles of 5.0, 8.0, and 12.0 degrees (figure IV.2 c,d, and e), the pressure coefficient drops as the chordwise position increases. This trend is mostly pronounced between

X/C = 0.40 to 0.90 at Z/S = 0.99, 0.97, and 0.96. This region corresponds to the area where the tip vortex is rolling up and the reduction in C_p is probably a result of an increase in the strength of the vortex. For example, at an angle of 5 degrees and Z/S = 0.99, C_p drops from -0.20 to -0.80 as X/C increases from 0.40 to 0.85, respectively. Similarly, at an angle of 8 degrees and a spanwise location of 0.99, the value of the pressure coefficient drops from -0.40 to -1.16 as the chordwise position increases from 0.40 to 0.85. The lowest values of C_p are measured at a 12^o incidence angle. At Z/S = 0.97, the pressure coefficient drops from -.52 to -1.80 as X/C changes from 0.40 to 0.85. This finding agrees with the trends observed during the flow visualization studies concerning the growth of the tip vortex with increasing incidence angles (see figure III.8). It is interesting to note that the trends observed on the suction side of the foil are also noticeable on the edge of the foil. As shown in figure IV.4, the value of C_p at an 8^o incidence drops from -1.08 to -1.42 as the chordwise position changes from 0.40 to 0.85.

The effects of the hydrofoil attachment device and support system are clearly evident in the pressure distributions near the root of the the foil. For example, at a 5^o incidence, Z/S = 0.39, and X/C = 0.05, the pressure coefficient drops to a minimum value of -1.14 (see figure IV.2 c). However, closer to the root, at Z/S = 0.14, C_p remains

at approximately -0.45 from X/C = 0.05 to 0.10. Similarly, at an angle of 8 degrees, Z/S = 0.06, and X/C = 0.05, the pressure coefficient levels off at a value close to -0.84, while at a location closer to the mid span, (Z/S = 0.31), and the same chordwise position, the pressure value drops to -1.44. The "flattening" of the surface pressure distribution near the root section is probably related to the flow interference caused by the fuselage which covers the attachment and support system of the hydrofoil.

The present results demonstrate clearly that the region with the lowest surface pressure is found in downstream locations near the tip of the foil. For example, at an angle of 12 degrees the minimum value of C_p, -1.8, is measured at X/C = 0.82 and Z/S = 0.97 (see figure IV.2 e). Similarly, at an angle of 8 degrees , the lowest surface pressure coefficient, -1.2, occurs at a chordwise position of 0.88 and a spanwise location of 0.97. Outside the tip region, near the mid span of the foil, the pressure coefficient reaches a minimum close to the leading edge. For example, at an angle of 8 degrees, C_p is -1.44 at X/C = 0.05 and Z/S = 0.31. Similarly , at a 5^o incidence , a chordwise position of 0.05, and a spanwise location of 0.39, the pressure coefficient is -1.14.

At incidence angles of 0 and 2 degrees, the lowest pressure coefficients are measured near the leading edge of

the foil, away from the tip region. For example, at 0^{o}, C_p reaches a minimum value of -0.70 at X/C = 0.50 and Z/S = 0.39 (figure IV.2 a). The deviations present in the distributions for low angles of incidence (in the regions beyond Z/S = 0.7) are related to the counter-rotating vortices that are observed under these conditions. Researchers such as Mueller (1986) have also obtained strange pressure distributions for NACA-66 profiles at low incidence angles. As mentioned previously, Mueller recorded negative lift coefficients for this foil at an incidence angle of 1 degree. When his results for mid span locations are compared to our results near this region, the distributions match well for higher incidence angles, (5^{o}, 8^{o}, and 12^{o}). In this case, the regions of boundary layer separation and the general shape of the surface pressure distributions are in agreement. However, at lower incidence angles, (0^{o} and 2^{o}), the distributions do not agree. In this case, Mueller's plots show that a dip in the pressure coefficient occurs near X/C = 0.05. In our graphs, the pressure distributions show a gradual decrease in the pressure coefficient as the chordwise position increases up to X/C = 0.50 (see figure IV.2 (a),(b)).

4.4 Boundary layer separation

Boundary layer separation becomes clearly evident in some of the surface pressure distributions. Its location is

determined when an inflection region (or point) follows a major dip in the pressure distribution. For example, at an 8^{o} incidence, boundary layer separation occurs at X/C = 0.20 (as indicated in figure IV.2). The pressure coefficient within the separation region varies between -0.96 and -0.58 depending on the spanwise location. Similarly, at a larger angle of 12^{o}, boundary layer separation occurs at X/C = 0.15, and the pressure coefficient within the separation region varies between -1.36 and -0.78. This example demonstrates that the value of C_p at separation increases with increasing angles of incidence. Also, it shows that the separation region on the foil occurs further upstream as the incidence angle increases.

Although separation occurs over a large portion of the surface of the foil, it is easily detected only at mid span positions. At large values of Z/S, the effects of the tip vortex become dominant and the flow becomes three dimensional. The interaction between the tip vortex and the separation region is an important subject for further study. Similarly, figures IV.2 c, and IV.2 d show that separation is suppressed also near the foil's root (near Z/S = 0.14 at 5^{o} and 8^{o} incidences, for example). The extent of the fuselage effect, however, depends on the incidence angle. For example, at a 12^{o} incidence, and Z/S = 0.14, separation is evident at X/C = 0.13, whereas no

clear signs of separation are evident at the same chordwise location at smaller angles.

It should be noted that, in this Reynolds Number range, the surface pressure distributions of the hydrofoil are very sensitive to changes in the flow conditions. Slight changes in the Reynolds Number could significantly effect boundary layer seperation.

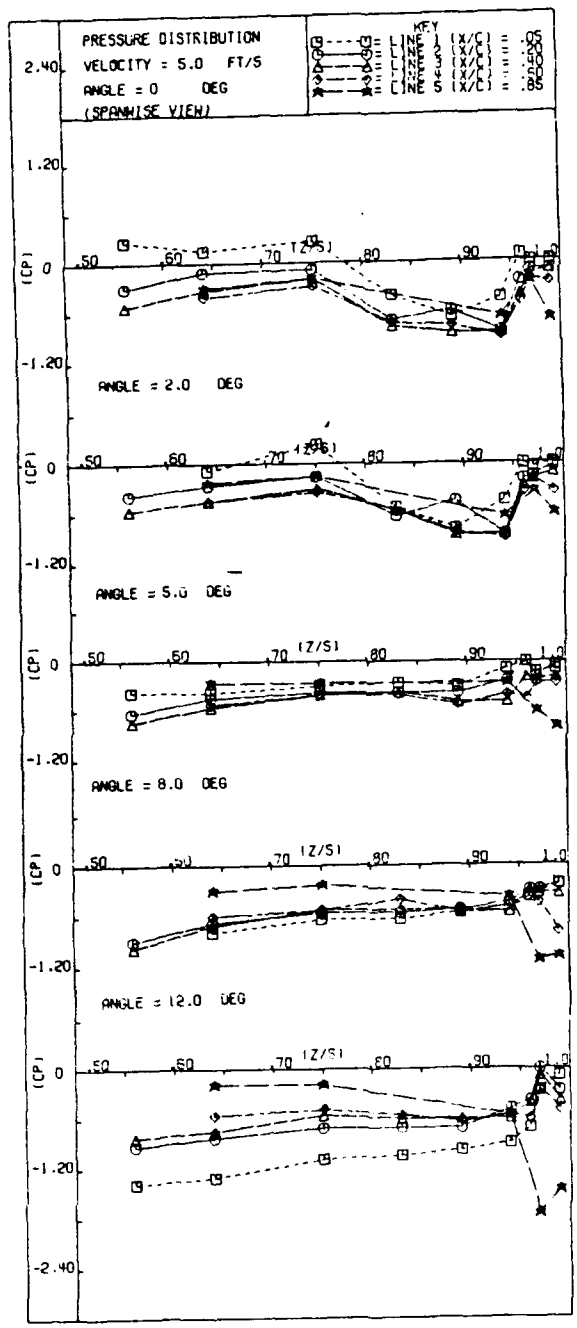

Figure IV.1 Spanwise distributions of the surface pressure coefficient on the hydrofoil.

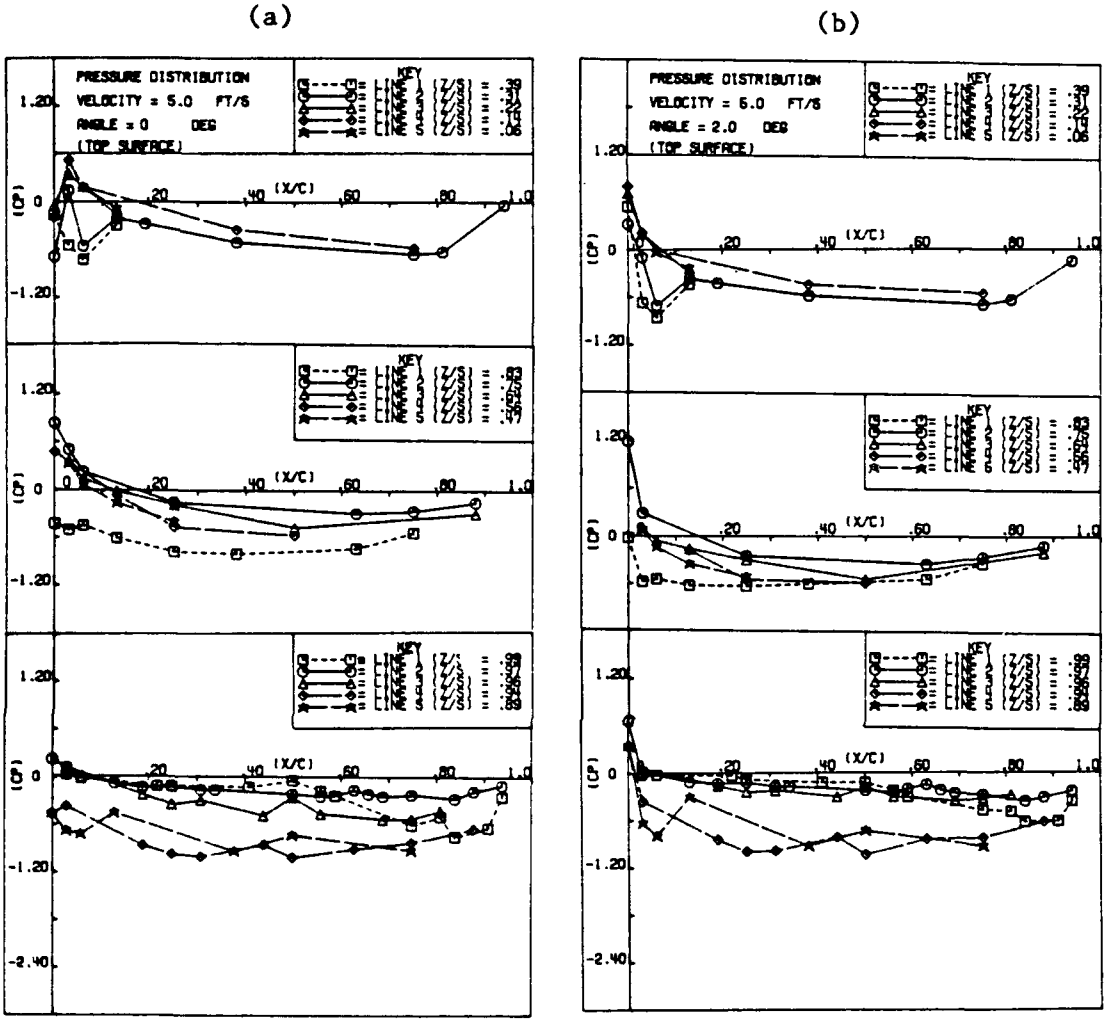

Figure IV.2 Chordwise distributions of the surface pressure coefficient on the hydrofoil (suction side).

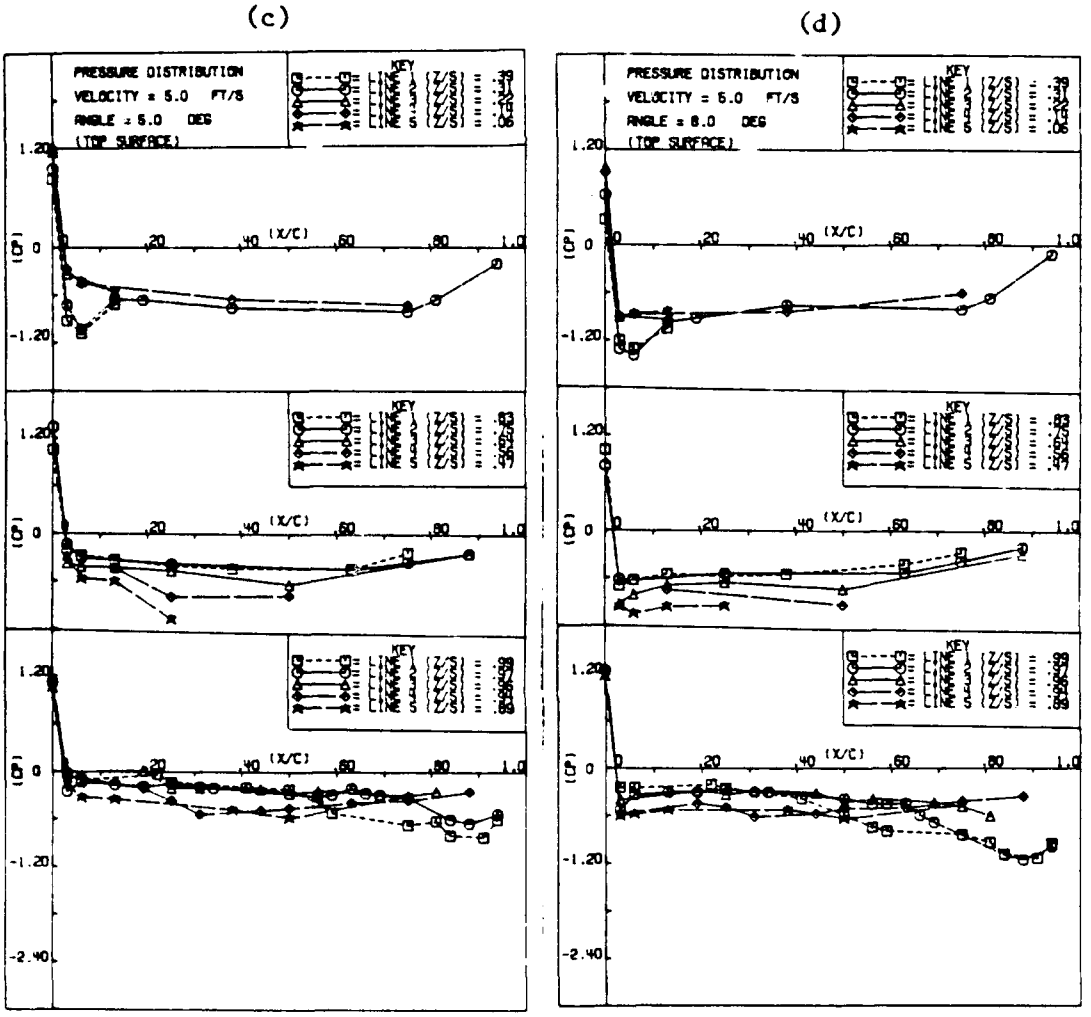

Figure IV.2, continued.

(e)

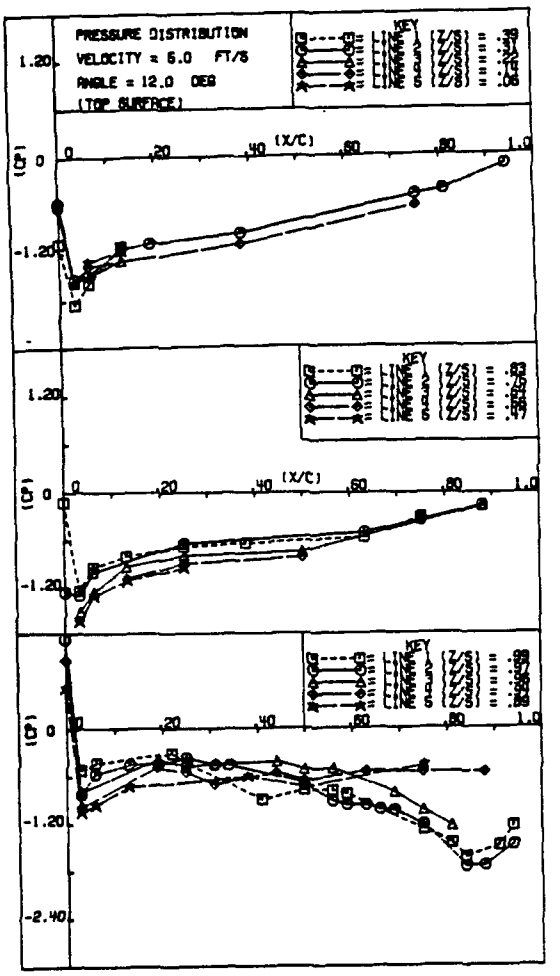

Figure IV.2, continued.

(a) (b)

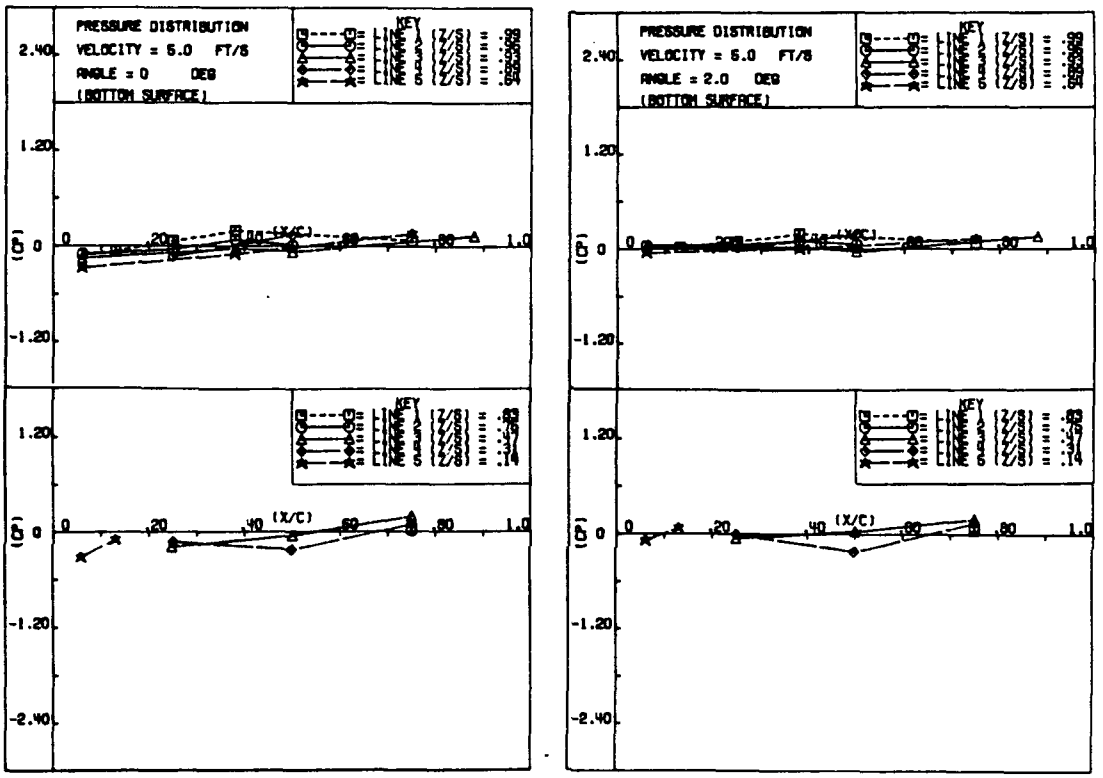

Figure IV.3 Chordwise distributions of the surface pressure coefficient on the hydrofoil (pressure side).

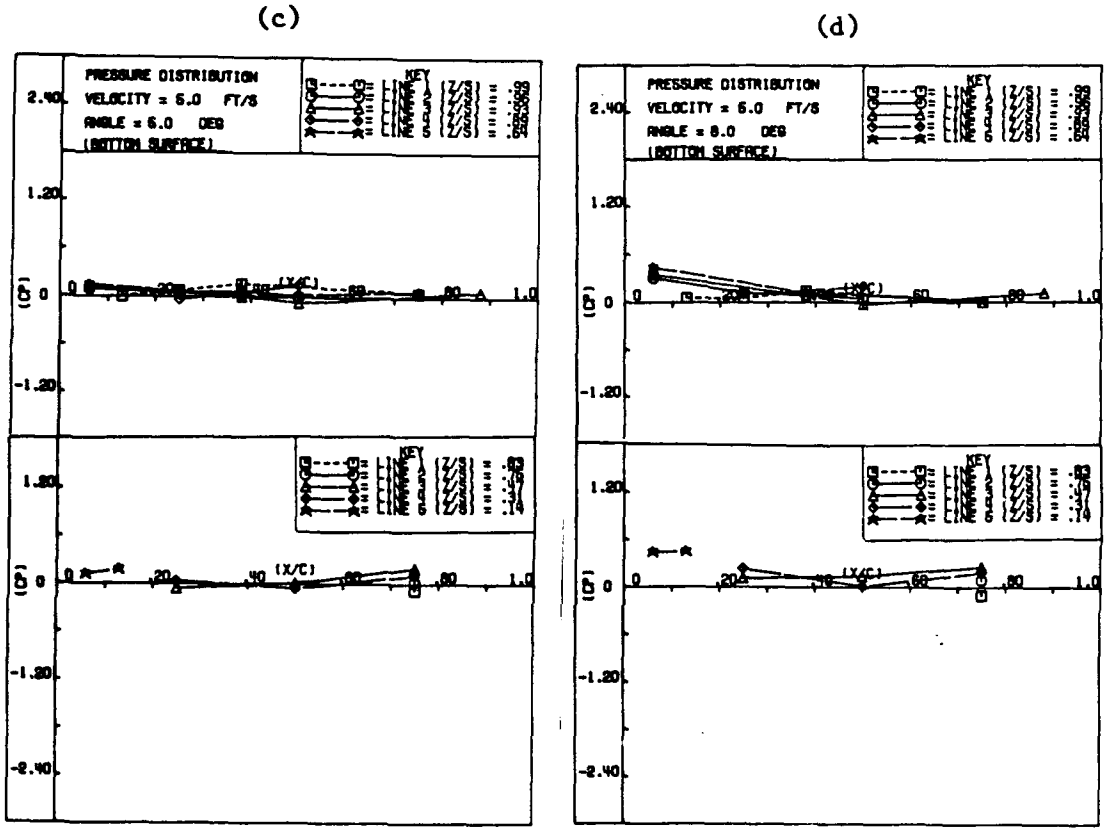

Figure IV.3, continued.

(e)

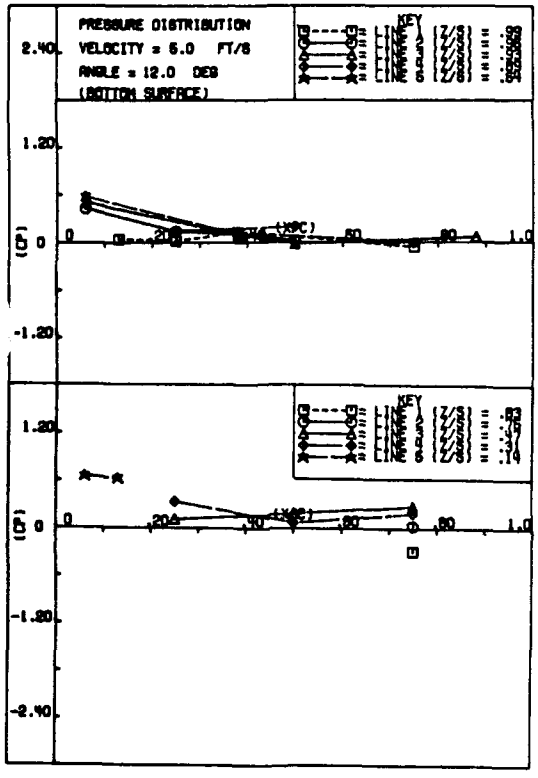

Figure IV.3, continued.

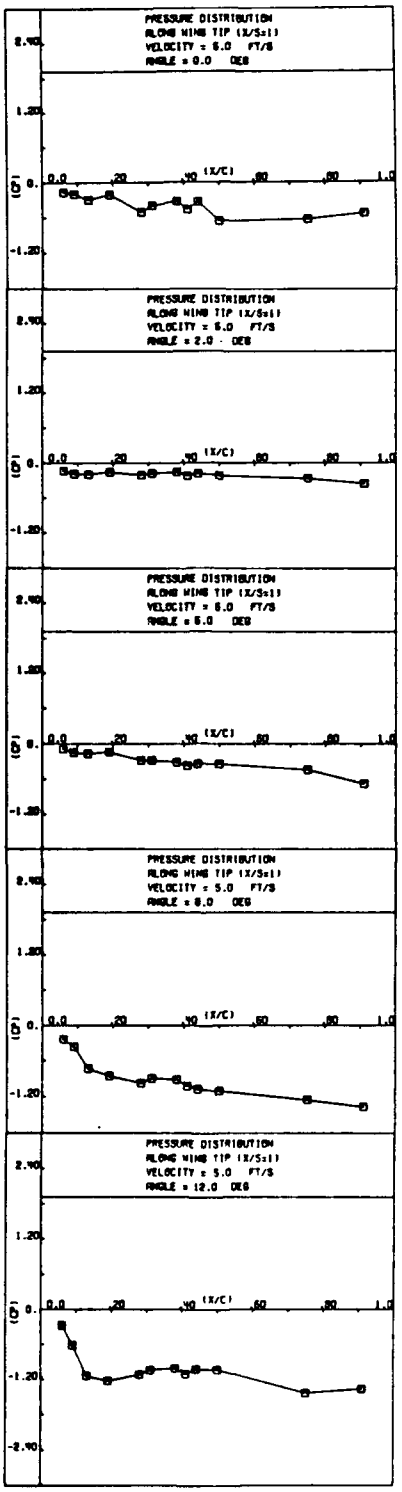

Figure IV.4 Distributions of the pressure coefficient along the hydrofoil's edge.

CHAPTER 5 - CONCLUSIONS AND RECOMMENDATIONS

5.1 Conclusions

A study of the roll up process of tip vortices is being performed on a NACA-66 series hydrofoil in a towing tank. Laser induced fluorescence is utilized as the method of flow visualization. A scanning procedure is used to obtain the surface pressure distribution.

A vast amount of information is processed to obtain quantified results from the flow visualization images. The observations made are used to demonstrate the growth of the tip vortex with increasing incidence angle, increasing chordwise location, and decreasing velocity. They show that the center of the vortex and the horizontal location of the attachment line move inward with increasing incidence angle, increasing chordwise location, and decreasing velocity. Empirical relations for these trends are presented. Observations of secondary structures are also noted.

Results obtained from the surface pressure measurements help in supplementing the flow visualization results. Spanwise pressure distributions document the

existence of a lateral pressure gradient that increases as the incidence angle increases. This trend implies an increase in the spanwise flow into the tip vortex, a phenomenon clearly substantiated by the flow visualization studies. Dips present in the spanwise pressure distributions are attributed to the presence of the tip vortex and a counter-rotating secondary vortex structure. The magnitude of the dip caused by the tip vortex increases as the chordwise position increases. An increase in the incidence angle reduces the effect of the secondary structures and increases the magnitude of the pressure dip associated with the tip vortex. The same pressure dips are also visible in the chordwise pressure distributions. Of particular importance is the gradual decrease in C_p near the tip with increasing chordwise position. The lowest surface pressure is measured near the tip region close to the trailing edge. Boundary layer separation is also evident in the chordwise distributions at incidence angles larger than 5^o. Near the mid span, separation occurs close to X/C = 0.20, and the separation point moves upstream as the incidence angle increases. Outside the mid span region, the flow becomes three dimensional, and the classical traces of two dimensional separation are no longer evident.

5.2 Recommendations

Future studies should focus primarily on two parameters affecting the roll up process of tip vortices. Firstly, the effect of the wing load distribution should be observed by visualizing the flow on other hydrofoil sections (such as those with elliptical and spherical planforms). Secondly, the effect of the boundary layer on the vortex roll up process should be carefully observed. To perform these observations, the experiments should be repeated using boundary layer tripping (which can be achieved by adding roughness to the surface) and using a second, chordwise, laser sheet for observing phenomena such as separation, transition, etc. High speed photography and multi-colored dye would also increase the observation capabilities.

An additional improvement to the current flow visualization system involves the incorporation of a system which would allow quantitative information to be extracted from the flow visualization images. This would be used to obtain the instantaneous velocity field around the wing tip in order to determine its circulation under various flow conditions. Several steps are required in order to perform this task. Firstly, the image recording time must be controlled and monitored accurately either by pulsing the light source illuminating the model, or by controlling the

exposure time of the camera. Secondly, the dye currently used must be replaced by fluorescing particles so that their traces will leave clear and separate impressions on the recording medium. Thirdly, the image must be analyzed, and the length of the particle traces must be measured carefully to determine their instantaneous velocity. To perform this measurement, the image must be digitized and fed into a computer for analysis. A relatively simple modification to the current procedure of recording an image, and the addition of digitizing capabilities to the video recorder would enable this procedure to be implemented. Specifically, a frame-storing device and computer boards that connect the video recorder to the IBM-PC-AT should be purchased. This addition would enable any desired frame of the flow visualization image to be digitized, manipulated, and traced in order to get the velocity values. Figure 5.1 includes an example of a digitized image and the photograph that it is generated from. Although the photograph is recorded without controlling the exposure time (i.e. the length of the traces), it still demonstrates the clarity and resolution possible when an image is manipulated by a computer. This computer generated image is recorded from the 4 x 5 photograph by using an Eikonix Camera, a Gould-Dianza processing system, softwear developed at Purdue University, and a VAX 11/780

computer (part of the Purdue University Engineering Computer Network). The digitizing process was performed by Professor Edward Delb (School of Electrical Engineering) with the help of Professor Jeffery Wright (School of Civil Engineering). It should be noted that the proposed system is simpler and much more accessible than the one used to generate the example shown.

Improvements can also be made in the pressure measurement system. Performing the measurements is a complicated part of foil testing. A simpler method of measuring pressures involves the use of the wind tunnel located in the hydraulics laboratory. Wind tunnel testing would eliminate the need for the pneumatic control system and the air-water interface set-up. Their elimination would help to make the pressure measuring process much easier.

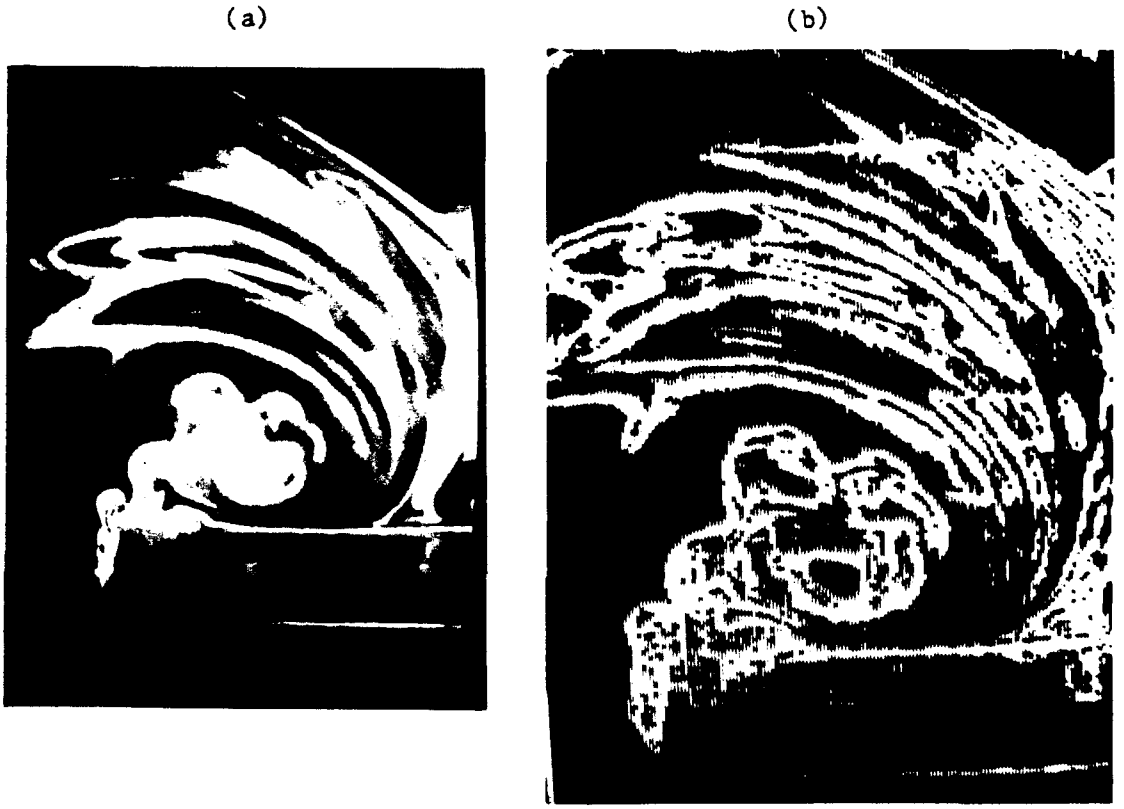

Figure V.1 A comparison between a photographic record, (a), and its digitized image. (b). The image digitization was performed by Professor Delb with an Eikonix camera and Gould Dianza Softwear/Hardwear.

BIBLIOGRAPHY

BIBLIOGRAPHY

1. Arakeri, V. H., Lodha, R. K., Mani, K., Munjal, M. L., (1982), "Cavitation Noise and Inception From a Model Propeller.", ASME International Symposium on Cavitation Noise.

2. Arndt, R. E. A., Higuchi, H., Quadrelli, C. S., (1985), "Tip Vortex Cavitation.",ASME Cavitation and Multi-Phase flow forum, FED - Vol.23.

3. Batchelor, G. K., (1964), "Axial Flow in Trailing Line Vortices.", Journal of Fluid Mechanics, vol. 20, part 4, pp. 645-658.

4. Betz, A., (1933), "Behavior of Vortex Systems.", NACA TM 713 (Translated from ZAMM, Vol. XII, 3, June, 1932).

5. Bilanin, A. J., Teske, M. E., Williamson, G. G., (1977), "Vortex Interactions and Decay in Aircraft Wakes.", AIAA Journal, vol. 15, No. 2, pp. 250-260.

6. Billet, M. L., (1975), "Surface and Tip Vortex Cavitation on a Family of Rectangular Foils", Applied Research Laboratory, Pennsylvania State University.

7. Bosswell, R. J., (1971), "Design, Cavitation Performance, and Open-Water Performance of a Series of Research Skewed Propellers.", NSRDC, Rep. No. 3339.

8. Brashears, M. R., Hallock, J. N., (1975), "Analysis of Predicted Aircraft Wake Vortex Transport and Comparison with Experiment.", Journal of Aircraft, Engineering Notes, vol. 12, no. 7, pp. 619-620.

9. Cebeci, T., Clark, R. W., Chang, K. C., Halsey, N.D., Lee, K., (1986), "Airfoils With Separation and the Resulting Wakes.", Journal of Fluid Mechanics, vol. 163, pp. 323-347.

10. Chandrashebhara, N., (1976), "Analysis of Tip Vortex Cavitation Inception of Hydrofoils and Propellers.", Hamburgische Schiffbau- Versuchsanstalt. Gmbh.

11. Chen, Z. L., Wu, J. M., (1983), "Jet Wing Vortex Lattice Theory With Nonlinear Wake and Tip Flows.", AIAA paper no. 83-0263.

12. Childs, R. E., (1986), "Lift Augumentation Via Spanwise Tip Blowing: A Numerical Study.", AIAA paper no. 86-0474.

13. Corsiglia, V. R., Schwind, R. G., Chigier, N. A., (1973), "Rapid Scanning, Three Dimensional Hot Wire Anemometer Surveys of Wing Tip Vortices.", Journal of Aircraft, vol. 10, no. 12, pp. 752-757.

14. Corsiglia, V. R., Rossow, V. J.,Ciffone, D. L., (1976), "Experimental Study of the Effect of Span Loading on Aircraft Wakes.", Journal of Aircraft, vol. 13, no. 12, pp. 968-973.

15. Crimi, P., (1970), "Experimental Study of the Effects of Sweep on Hydrofoil Loading and Cavitation.", Journal of Hydronautics, vol. 4, no. 1, pp. 3-9.

16. Dewey, F. C., (1976), "Qualitative and Quantitative Flow Field Visualization Utilizing Laser-Induced Fluorescence.", AGARD-CP- 193, no. 17.

17. Donaldson, C. du P., (1971), "A Brief Review of the Aircraft Trailing Vortex Problem.", AFOSR TR-71-1910.

18. Donaldson, C. du P., Snedeker, R. S., Sullivan, R. D., (1973), "Calculation of the Wakes of Three Transport Aircraft in Holding, Takeoff, and Landing Configurations and Comparison With Experimental Measurements.", FAA-RD-73-42, Washington, D.C.

19. Donaldson, C. du P., Bilanin, A. J., (1975), "Vortex Wakes of Conventional Aircraft.", AGARD-AG-204.

20. El-Ramly, Z., Rainbird, W. J., (1977), "Flow Survey of the Vortex Wake Behind Wings.", Journal of Aircraft, vol. 14, no. 11, pp. 1102-1108.

21. Eppler, R., Shen, Y. T., (1979), "Wing Section for Hydrofoils- Part 1: Symmetric Profiles.", Journal of Ship Research, vol. 23, no. 3, pp. 209-217.

22. Francis, M., (1976), "A Wind Tunnel Investigation of the Formation of a Trailing Vortex.", University of Colorado, Ph.D. Thesis, Aeronautical Engineering.

23. Freymuth, P., Bank, W., Palmer, M., (1984), "Vortices Around Airfoils.", American Scientist, vol. 72, pp.242-248.

24. Freymuth, P., Bank, W., Palmer, M., (1985), "Reynolds Number Dependence of Vortex Patterns in Accelerated Flows Around Airfoils.", Experiments in Fluids, vol. 3, pp. 109-112.

25. Freymuth, P., Bank, W., Finaish, F., (1985), "Visualization of the Spanwise Vortex Structure in the Starting Flow Behind an Airfoil.", AIAA paper no. 85-0447.

26. Freymuth, P., Finaish, F., Bank, W., (1986), "Visualization of Wing Tip Vortices in Unsteady and Steady Wind.", AIAA paper no. 86-1096.

27. Gostelow, J. P., Wong, K. K., (1985), "Observations of Impeller Tip Cavitation in an Axial Flow Pump.", ASME Cavitation and Multi-Phase Flow Forum, FED-vol. 23.

28. Grow, T. L., (1969), "Effect of a Wing on its Tip Vortex.", Journal of Aircraft, vol. 6, no. 1, pp. 37-41.

29. Hallock, J. N., Eberle, W. R., (1977), "Aircraft Wake Vortices: A State of the Art Review of the United States Research and Development Program.", F.A.A.-RD-77-23.

30. Higuchi, H., Taghani, R., Arndt, R. E. A., (1985), "Sound Source Location in Cavitating Tip Vortices.", ASME Cavitation and Multi Phase Flow Forum, FED-vol. 23.

31. Higuchi, H., Quadrelli, J.C., Farell, C., (1986), "Vortex Roll-Up for an Elliptically-Loaded Wing at Moderately Low Reynolds Numbers.", AIAA report no. 86-0562.

32. Kuiper, G. ,(1979), "Modeling of Tip Vortex Cavitation on Ship Propellers.", 4th Lips Propellers Symposium, Drunen, The Netherlands.

33. Lamb, H., (1932), Hydrodynamics, Cambridge, also Dover edition, New York, 1945.

34. Loth, J. L., Loth, F., (1984), "Induced Drag Reduction with Wing Tip Mounted Propellers.", AIAA paper no. 84-2149.

35. Mansour, N. N., (1984), "Numerical Simulation of the Tip Vortex off a Low-Aspect Ratio Wing at Transonic Speeds.", AIAA paper no. 84-522.

36. McCormick, B. W., (1962), "On Cavitation Produced by a Vortex Trailing From a Lifting Surface.", Journal of Basic Engineering, pp. 369-379.

37. McCormick, B. W., Tangler, J. L., Sherrieb, H. E., (1968), "Structure of Trailing Vortices.", Journal of Aircraft, vol. 5, no. 3, pp. 260-267.

38. Mertaugh, L. J., Damania, R. B., (1977), "An Investigation of the Near- Field Wake Behind a Full Scale Test Aircraft.", Journal of Aircraft, vol. 14, no. 9, pp. 894-902.

39. Moore, D. W., Saffman, P. G., (1973), "Axial Flow in Laminar Trailing Vortices.", Proc. Royal Society of London, A.333, pp. 491-508.

40. Mueller, T. J., Private Communication, (1986).

41. Murai, H., Ihara, A., Tsursimi, Y., (1979), "Cavitation on Hydrofoils in Turbulent Shear Flow.", Twelfth Symposium on Naval Hydrodynamics, Washington, D.C.

42. Palmer, P., Freymuth, P., (1984), "Analysis of Vortex Development From Visualization of Accelerating Flow Around an Airfoil, Starting From Rest.", AIAA paper no. 84-1568.

43. Platzer, G. P., Sounders, W. G., (1979), "Tip Vortex Cavitation Delay With Applications to Mrine Lifting Surfaces, A Literature Survey.", David Taylor Naval Ship Research and Development Center rep. no. 779/051.

44. Shamroth, S. J., Gibeling, H. J., (1979), "A Compressible Solution of the Navier-Stokes equations for Turbulent Flow About an Airfoil.", NASA-CR-3183.

45. Shen, Y. T., Eppler, R., (1981), "Wing Sections for Hydrofoils - Part 2: Nonsymmetric Profiles.", Journal of Ship Research, vol. 25, no. 3, pp. 191-200.

46. Shen, Y. T., (1985), "Wing Sections for Hydrofoils - Part 3: Experimental Verifications.", Journal of Ship Research, vol. 29, no. 1, pp. 39-50.

47. Sounders, W. G., Platzer, G. P., (1981), "Tip Vortex Cavitation Characteristics and Delay of Inception on a Three Dimensional Hydrofoil.", David Taylor Naval Ship Research and Develpment Center, rep. no. 81/007.

48. Tavella, D. A., Wood, N. J., (1985), "Influence of Tip Blowing on Rectangular Wings.", AIAA paper no. 85-5001.

49. Thompson, D. H., (1975), "Experimental Study of Axial Flow in Wing Tip Vortices.", Journal of Aircraft, Vol.12, No. 11, Engineering Notes, pp. 911-914.

50. Wu, J. M., Vakili, A. D., (1984), "Aerodynamic Interactions of Wingtip Flow With Discrete Wingtip Jets.", AIAA paper no. 84-2206.

51. Yates, E. J., (1974), "Calculation of Initial Vortex Roll-Up in Aircraft Wakes.", Journal of Aircraft, vol. 11, no. 7, pp. 397-400.

APPENDICES

Appendix A : Wing profile information

Table A.1 Wing profile information

NACA-66 (DTMB MODIFIED) GEOMETRY		
STATION (X) (inches)	TOP ORDINANT (inches)	BOTTOM ORDINANT (inches)
0	0	0
0.12	0.18	-0.13
0.18	0.23	-0.16
0.30	0.30	-0.20
0.60	0.45	-0.26
1.20	0.66	-0.33
1.80	0.83	-0.39
2.40	0.97	-0.43
3.60	1.20	-0.49
4.80	1.38	-0.54
6.00	1.52	-0.57
7.20	1.63	-0.59
8.40	1.71	-0.61
9.60	1.77	-0.61
10.80	1.79	-0.61
12.00	1.79	-0.59
13.20	1.76	-0.56
14.40	1.70	-0.53
15.60	1.62	-0.49
16.80	1.50	-0.43
18.00	1.35	-0.38
19.20	1.17	-0.32
20.40	0.93	-0.28
21.60	0.67	-0.24
22.80	0.38	-0.17
24.00	0.08	-0.08

NOTE:

LEADING EDGE RADIUS = .448*(t/c)*(t/c)*C

=.448*(.10)*(.10)*24inches = .1075 inches

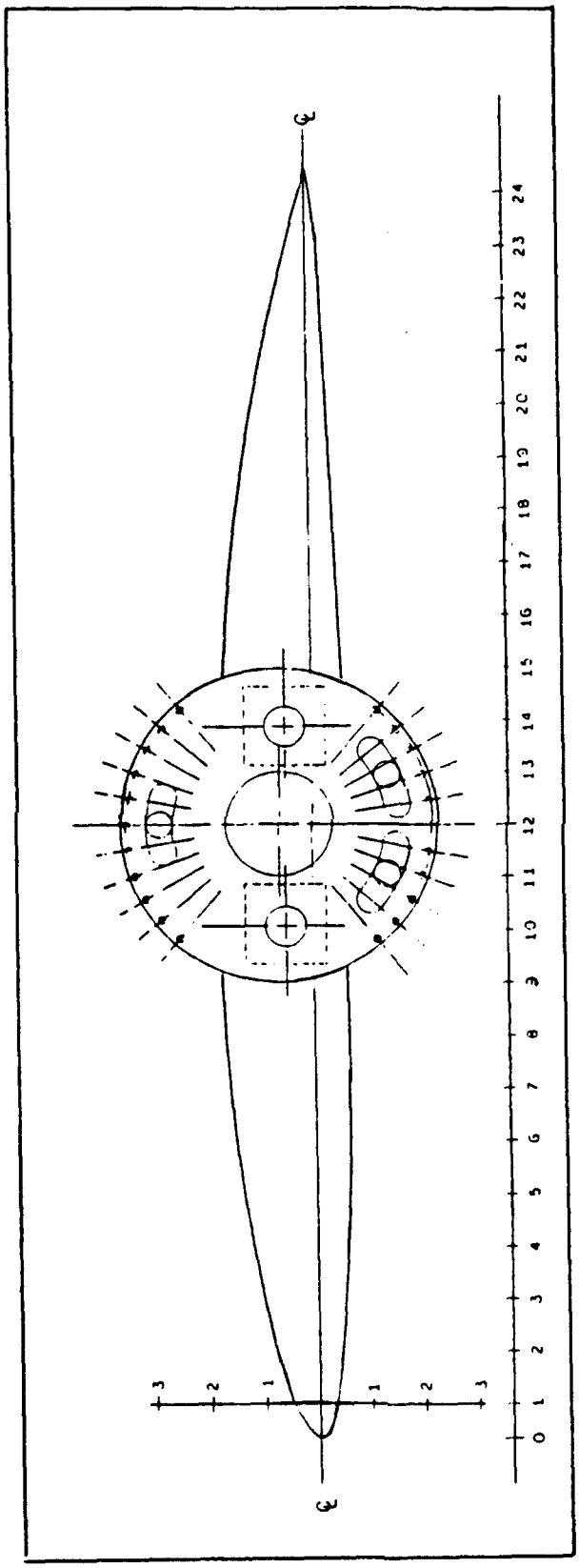

Figure A.1 A drawing of a cross section of the NACA-66 hydrofoil used in the present study.

Appendix B : Pressure measurement data

Table B.1 A sample of the pressure measurement data

Angle = 0. degrees Velocity = 5. ft/sec			Angle = 2. degrees Velocity = 5. ft/sec		
Cp	x/c	z/s	Cp	x/c	z/s
0.03	0.03	0.99	0.10	0.03	0.99
-0.02	0.06	0.99	-0.03	0.06	0.99
-0.11	0.22	0.99	-0.04	0.22	0.99
-0.11	0.25	0.99	-0.09	0.25	0.99
-0.12	0.41	0.99	-0.13	0.41	0.99
-0.04	0.50	0.99	-0.13	0.50	0.99
-0.17	0.56	0.99	-0.23	0.56	0.99
-0.23	0.59	0.99	-0.31	0.59	0.99
-0.60	0.75	0.99	-0.48	0.75	0.99
-0.50	0.81	0.99	-0.50	0.81	0.99
-0.75	0.84	0.99	-0.63	0.84	0.99
-0.64	0.91	0.99	-0.62	0.91	0.99
-0.25	0.94	0.99	-0.37	0.94	0.99
0.22	0.00	0.97	0.66	0.00	0.97
0.12	0.03	0.97	-0.03	0.03	0.97
0.00	0.06	0.97	-0.03	0.06	0.97
-0.08	0.13	0.97	-0.12	0.13	0.97
-0.13	0.19	0.97	-0.14	0.19	0.97
-0.12	0.25	0.97	-0.13	0.25	0.97
-0.16	0.31	0.97	-0.18	0.31	0.97
-0.16	0.34	0.97	-0.18	0.34	0.97
-0.21	0.50	0.97	-0.23	0.50	0.97
-0.24	0.56	0.97	-0.26	0.56	0.97
-0.23	0.59	0.97	-0.21	0.59	0.97
-0.16	0.63	0.97	-0.16	0.63	0.97
-0.21	0.66	0.97	-0.23	0.66	0.97
-0.24	0.69	0.97	-0.27	0.69	0.97
-0.22	0.75	0.97	-0.29	0.75	0.97
-0.27	0.84	0.97	-0.37	0.84	0.97
-0.18	0.88	0.97	-0.32	0.88	0.97
-0.10	0.94	0.97	-0.24	0.94	0.97

Table B.1, continued.

Angle = 12. degrees Velocity = 5. ft/sec		
Cp	x/c	z/s
-0.52	0.03	0.99
-0.43	0.06	0.99
-0.31	0.22	0.99
-0.43	0.25	0.99
-0.90	0.41	0.99
-0.78	0.50	0.99
-0.79	0.56	0.99
-0.83	0.59	0.99
-1.28	0.75	0.99
-1.46	0.81	0.99
-1.63	0.84	0.99
-1.49	0.91	0.99
-1.24	0.94	0.99
1.14	0.00	0.97
-0.82	0.03	0.97
-0.57	0.06	0.97
-0.45	0.13	0.97
-0.44	0.19	0.97
-0.37	0.25	0.97
-0.46	0.31	0.97
-0.46	0.34	0.97
-0.69	0.50	0.97
-0.92	0.56	0.97
-0.97	0.59	0.97
-0.97	0.63	0.97
-1.03	0.66	0.97
-1.04	0.69	0.97
-1.22	0.75	0.97
-1.75	0.84	0.97
-1.74	0.88	0.97
-1.48	0.94	0.97

Table B.1, continued.

Angle = 5. degrees Velocity = 5. ft/sec			Angle = 8. degrees Velocity = 5. ft/sec		
Cp	x/c	z/s	Cp	x/c	z/s
-0.04	0.03	0.99	-0.25	0.03	0.99
-0.11	0.06	0.99	-0.25	0.06	0.99
-0.04	0.22	0.99	-0.21	0.22	0.99
-0.14	0.25	0.99	-0.26	0.25	0.99
-0.20	0.41	0.99	-0.39	0.41	0.99
-0.22	0.50	0.99	-0.60	0.50	0.99
-0.39	0.56	0.99	-0.75	0.56	0.99
-0.52	0.59	0.99	-0.80	0.59	0.99
-0.67	0.75	0.99	-0.84	0.75	0.99
-0.62	0.81	0.99	-0.94	0.81	0.99
-0.80	0.84	0.99	-1.09	0.84	0.99
-0.82	0.91	0.99	-1.14	0.91	0.99
-0.60	0.94	0.99	-0.95	0.94	0.99
1.12	0.00	0.97	1.23	0.00	0.97
-0.26	0.03	0.97	-0.53	0.03	0.97
-0.14	0.06	0.97	-0.34	0.06	0.97
-0.17	0.13	0.97	-0.31	0.13	0.97
-0.19	0.19	0.97	-0.31	0.19	0.97
-0.16	0.25	0.97	-0.27	0.25	0.97
-0.19	0.31	0.97	-0.31	0.31	0.97
-0.21	0.34	0.97	-0.31	0.34	0.97
-0.28	0.50	0.97	-0.39	0.50	0.97
-0.31	0.56	0.97	-0.46	0.56	0.97
-0.29	0.59	0.97	-0.46	0.59	0.97
-0.21	0.63	0.97	-0.45	0.63	0.97
-0.27	0.66	0.97	-0.60	0.66	0.97
-0.29	0.69	0.97	-0.69	0.69	0.97
-0.33	0.75	0.97	-0.85	0.75	0.97
-0.60	0.84	0.97	-1.10	0.84	0.97
-0.65	0.88	0.97	-1.16	0.88	0.97
-0.53	0.94	0.97	-0.99	0.94	0.97

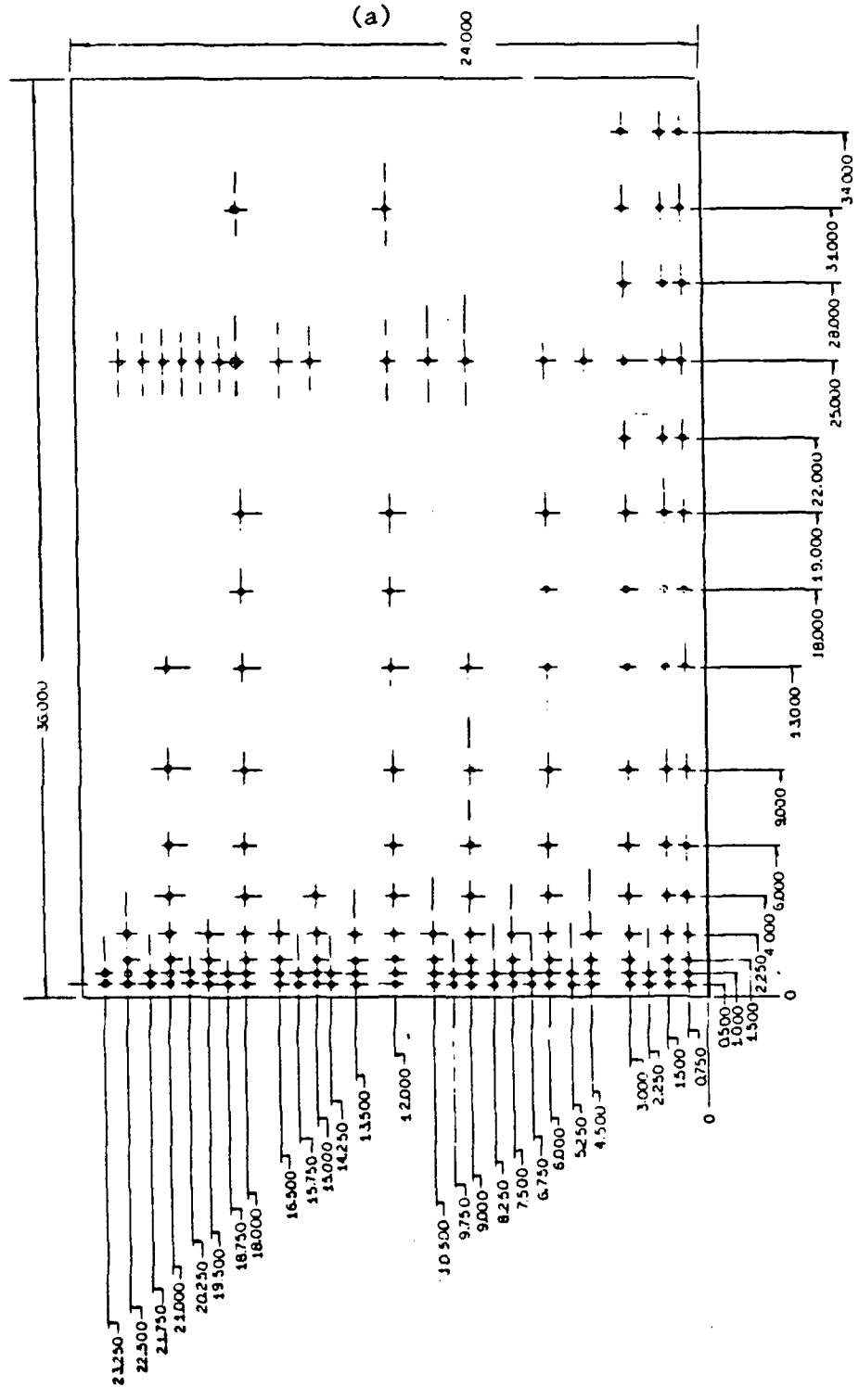

Figure B.1 The location of the pressure taps on the surface of the hydrofoil.
(a) suction side
(b) pressure side

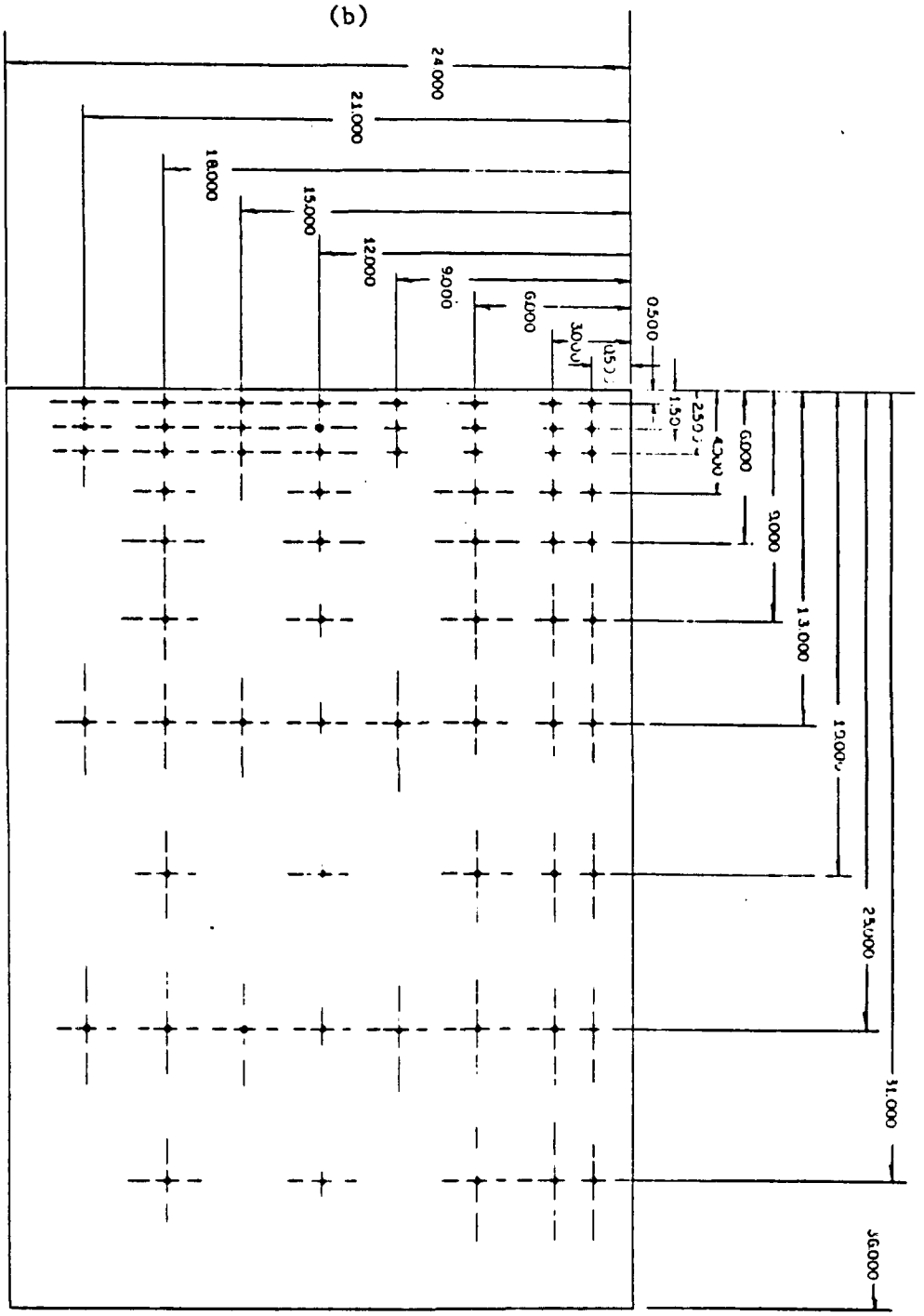

Figure B.1, continued.

Appendix C : Flow visualization data

Table C.1 Flow visualization data

Angle Deg.	(x/c) Loc.	Speed ft/s	Vortex Rad. (in)	Cl X Loc. (in)	Cl Y Loc. (in)	Attach. line	2nd vort Radius	2nd Cl X Loc.	2nd Cl Y Loc.
0	0.46	1.0					0.164	-0.329	-0.345
0	0.46	2.0					0.148	-0.197	-0.296
0	0.46	3.0					0.140	-0.279	-0.263
0	0.46	5.0					0.132	-0.263	-0.214
0	0.46	0.5					0.197	-0.395	-0.115
0	0.83	1.0	0.120	0.209	0.104		0.333	1.333	0.667
0	0.83	2.0	0.052	0.104	0.104		0.333	0.667	0.667
0	0.63	1.0	0.104	0.229	0.250		0.104	-0.333	-0.333
0	0.63	2.0	0.083	0.167	0.209		0.125	-0.250	-0.250
0	0.63	3.0	0.083	0.167	0.167		0.125	-0.250	0.250
0	0.63	5.0	0.083	0.250	0.167		0.083	-0.167	0.250
0	0.85	1.0	0.250	0.500	0.250		0.333	1.000	0.833
0	0.85	2.0	0.167	0.333	0.250				
0	0.85	3.0	0.167	0.500	0.292		0.333	1.000	1.167
0	0.85	5.0	0.167	0.583	0.333		0.333	0.667	1.000
0	0.67	0.5	0.167	0.167	0.250		0.167	-0.250	0.167
0	0.67	1.0	0.167	0.250	0.167		0.333	-0.167	0.417
0	0.67	2.0	0.125	0.375	0.167		0.208	0.209	0.583
0	0.50	0.5					0.292	-0.333	-0.500
0	0.50	1.0					0.208	-0.250	-0.459
0	0.50	2.0					0.250	-0.333	-0.333
0	0.50	3.0					0.167	-0.250	0.000
0	1.00	2.0	0.417	0.750	0.667				
0	1.00	3.0	0.375	0.750	0.667	1.333	0.167	1.833	1.333
2	0.36	2.0					0.208	-0.125	-0.125
2	0.36	3.0					0.167	-0.167	-0.125
2	0.36	5.0					0.208	-0.209	-0.333
2	0.49	1.0	0.167	0.250	0.167		0.333	-0.167	0.292
2	0.49	2.0	0.125	0.125	0.167		0.167	-0.083	0.209
2	0.81	2.0	0.250	0.500	0.146				
2	0.81	3.0	0.208	0.583	0.333				
2	1.00	5.0	0.583	1.083	0.583	1.830	0.250	1.833	0.333
2	1.00	1.0	0.667	1.083	0.583	1.920			
2	1.00	2.0	0.583	0.833	0.583	2.080			
2	1.00	3.0	0.667	1.000	0.583	1.920			
2	0.70	1.0	0.250	0.333	0.333		0.333	-0.209	0.667
2	0.70	2.0	0.167	0.375	0.250		0.250	0.833	0.750
2	0.57	3.0	0.208	0.500	0.250		0.208	0.375	0.500
5	0.57	1.0	0.167	0.417	0.250	1.000	0.167	1.333	0.417
5	0.69	1.0	0.333	0.667	0.333	1.667	0.250	2.333	0.459
5	0.69	2.0	0.333	0.750	0.417	1.667	0.333	2.667	0.333
5	0.69	3.0	0.333	0.667	0.333	1.250	0.333	2.167	0.333
5	0.69	5.0	0.250	0.500	0.292	1.080	0.250	1.667	0.583
5	1.00	1.0	0.833	1.000	0.833	3.000			
5	1.00	3.0	0.833	0.917	0.750	3.000			
5	1.00	5.0	0.625	0.667	0.667				
5	0.92	5.0	0.500	0.833	0.500	2.000	0.500	2.833	0.667
5	0.92	0.5	0.833	0.917	0.500				
5	0.92	2.0	0.625	0.917	0.583	2.167			
5	0.92	1.0	0.708	1.000	0.625				
5	0.82	1.0	0.583	0.833	0.500	1.667	0.333	2.667	0.333
5	0.82	3.0	0.500	0.833	0.500	1.667			
5	0.82	5.0	0.333	0.833	0.417	1.500	0.333	2.000	0.792
5	0.50	1.0	0.125	0.250	0.125				
5	0.50	3.0	0.125	0.250	0.125				
5	0.83	0.5	0.313	0.750	0.500	1.750			
5	0.83	1.0	0.600	1.000	0.500	1.750			
5	0.83	2.0	0.375	0.750	0.500	1.750			
5	0.83	3.0	0.500	0.750	0.500	1.750			

Table C.1, condinued.

Angle Deg.	(x/c) Loc.	Speed ft/s	Vortex Rad. (in)	Cl X Loc. (in)	Cl Y Loc. (in)	Attach. line	2nd vort Radius	2nd Cl X Loc.	2nd Cl Y Loc.
8	0.64	0.5	0.263	0.625	0.263	2.333			
8	0.64	5.0	0.230	0.526	0.263				
8	0.64	1.0	0.333	0.917	0.459	2.250			
8	0.64	2.0	0.375	0.833	0.333	1.667			
8	0.64	3.0	0.333	0.833	0.375	1.825			
8	0.46	1.0	0.292	0.667	0.333	1.080			
8	0.46	2.0	0.188	0.417	0.250	1.080	0.125	1.750	0.250
8	0.46	3.0	0.188	0.417	0.250	1.167			
8	0.46	0.5	0.146	0.500	0.250				
8	0.68	0.5	0.375	0.875	0.500	3.000			
8	0.68	1.0	0.375	0.750	0.500	2.000	0.500	3.500	0.500
8	0.68	2.0	0.500	0.875	0.500	2.000			
8	0.68	3.0	0.438	0.875	0.500	2.000			
8	0.68	5.0	0.313	0.750	0.375	1.750			
8	0.49	0.5	0.219	0.625	0.250	1.500			
8	0.49	1.0	0.250	0.625	0.375	1.375			
8	0.49	2.0	0.156	0.500	0.250	1.250			
8	0.49	3.0	0.156	0.500	0.250	1.250			
8	0.49	5.0	0.125	0.375	0.188	0.933			
8	1.00	0.5	0.875	1.250	0.875	4.000			
8	1.00	3.0	0.813	1.125	0.875	3.500			
8	1.00	1.0	0.875	1.250	1.125	4.000			
8	1.00	5.0	0.750	0.750	1.000	3.000			
8	0.88	0.5	0.750	1.250	0.750	3.500			
8	0.88	1.0	0.750	1.250	0.750	4.000			
12	0.46	0.5	0.500	0.875	0.375	2.000			
12	0.46	1.0	0.250	0.709	0.333	1.667			
12	0.46	2.0	0.250	0.750	0.417	1.667			
12	0.46	3.0	0.250	0.583	0.292	1.333			
12	0.46	5.0	0.208	0.542	0.292	1.333			
12	0.61	0.5	0.583	1.333	0.500	2.667			
12	0.61	1.0	0.500	1.000	0.417	2.500			
12	0.61	2.0	0.500	1.083	0.583	2.333			
12	0.61	3.0	0.478	1.083	0.583				
12	0.61	5.0	0.375	0.917	0.500				
12	0.82	0.5	1.000	1.667	1.000	3.167			
12	0.82	1.0	0.646	1.167	0.667	3.000			
12	0.82	2.0	0.917	1.500	0.833				
12	0.82	3.0	0.917	1.500	0.833				
12	0.82	5.0	0.583	1.167	0.667				
12	0.88	2.0	1.000	1.500	0.875	4.000			
12	0.88	3.0	1.000	1.500	1.000	3.500			
12	0.88	5.0	0.625	1.125	0.750	3.000			
12	0.50	0.5	0.375	1.000	0.500	2.125			
12	0.50	1.0	0.313	0.875	0.500	2.000			
12	0.50	2.0	0.250	1.000	0.500	1.750			
12	0.50	3.0	0.219	0.875	0.375	1.500			

Appendix D : Uncertainty

There is a small degree of uncertainty in the flow visualization analysis section. Measured values of the tip vortex size and location varied slightly. To determine the error, measurements are taken of the tip vortex size and location from a series of images frozen during the same run, and also from several series of images frozen during different runs under the same flow conditions. For example, at $Re_c = 3.7 \times 10^5$, $\alpha = 2^o$, and X/C = 0.70, five measured dimensions of the tip vortex size are (D/C) = 0.014, 0.014, 0.014, 0.016, and 0.014. Five measured horizontal locations are (LZ/C) = 0.014, 0.014, 0.016, 0.016, 0.014. Five measured vertical locations are (LY/C) = 0.011, 0.011, 0.012, 0.011, 0.012. Similarly, at $Re_c = 5.6 \times 10^5$, $\alpha = 8^o$, and X/C = 0.11, five measured dimensions of the tip vortex size are (D/C) = 0.017, 0.016, 0.016, 0.017, 0.016. Five measured horizontal locations are (LZ/C) = 0.017, 0.017, 0.017, 0.017, 0.016. Five measured vertical locations are (LY/C) = 0.010, 0.010, 0.010, 0.010, 0.010.

From these distributions ,and from the series of other measurements, the standard deviation of (D/C) is +/- 0.004, while the standard deviation for (LZ/C) = +/- 0.003, and the standard deviation for (LY/C) = +/- 0.002. These values can serve as characteristic errors.